

1

2

3

4

Iron isotope insights into equatorial Pacific biogeochemistry

5

6 Authors: Capucine Camin ¹, Marie Labatut¹, Catherine Pradoux¹, James W. Murray², François
7 Lacan¹

8

9 ¹ Université de Toulouse, LEGOS (CNES/CNRS/IRD/UT), Toulouse, France

10 ² School of Oceanography, University of Washington, Seattle, Washington, USA

11

12 Corresponding authors: Capucine Camin and François Lacan, LEGOS, 14 Avenue Edouard
13 Belin, F-31400 Toulouse, France (capucine.camin@orange.fr and francois.lacan@cnrs.fr).

14

15

ABSTRACT

The EUCFe cruise (RV *Kilo Moana*, 2006) was designed to characterize sources of Fe to the western equatorial Pacific and its transport by the Equatorial Undercurrent (EUC), a narrow and fast eastward current flowing along the equator, to the eastern equatorial Pacific High Nutrient Low Chlorophyll (HNLC) region. This study presents seawater dissolved (DFe) and particulate (PFe) iron concentrations and isotopic compositions ($\delta^{56}\text{DFe}$ and $\delta^{56}\text{PFe}$) from 15 stations in the equatorial band (2°N-2°S) between Papua New Guinea and 140°W, over more than 8 500 km along the equator and in the upper 1 000 m of the water column.

$\delta^{56}\text{DFe}$ and $\delta^{56}\text{PFe}$ ranged from -0.22 to $+0.79 \pm 0.07$ ‰ and from -0.52 to $+0.43 \pm 0.07$ ‰, respectively (relative to IRMM-14, 95 % confidence interval). Source signatures, biogeochemical processes and transport all contribute to these observations. Two distinct areas, one under continental influence (the western equatorial Pacific) and an open ocean region (the central equatorial Pacific), emerged from the data. In the area under continental influence, high PFe concentrations along with $\delta^{56}\text{DFe}$ values systematically heavier than that of $\delta^{56}\text{PFe}$ indicated an equilibrium fractionation and the co-occurrence of chemical fluxes from both phases toward the other. This exchange occurs through non-reductive processes, as previously proposed from three of the eight stations of this area (Labatut et al., 2014) and extends up to 1 200 km from the coast. In the open ocean area, preservation of a DFe isotopic signature of $\sim +0.36$ ‰ within the EUC, from Papua New Guinea to the central equatorial Pacific (7 800 km), confirmed the origin of the DFe carried within this current toward the HNLC region. At the same depth, bordering the EUC at 2°N and 2°S at 140°W, light isotopic signatures suggested that iron was originating from the eastern Pacific oxygen minimum zones. These light signatures were also observed in deeper central waters, between 200 and 500 m. Our data did not allow conclusions about fractionation during uptake by phytoplankton, but indicated that any fractionation, if present, must be small, no larger than a few tenths of a per mil.

KEY WORDS

Iron isotopes, equatorial Pacific Ocean, oxygen minimum zones, non-reductive dissolution, iron cycle, water masses.

1. INTRODUCTION

Iron (Fe) is an essential nutrient for phytoplankton, enabling them to fulfil their role as primary producers (Morel et al., 2020). Through its influence on primary productivity and plankton speciation, Fe plays a critical role in regulating the biological carbon pump and, consequently, the global carbon cycle and climate. Fe concentrations in the surface open ocean are often low (of the order of 0.1 nmol.kg^{-1}), potentially limiting primary productivity (Martin, 1992). Regions where Fe is limiting, despite the availability of macronutrients, are termed High Nutrient Low Chlorophyll (HNLC) areas. One notable HNLC region is the eastern equatorial Pacific (Chisholm and Morel, 1991), where Fe is believed to have a main source from the western Pacific and transported eastward within the Equatorial Undercurrent (EUC) (Murray et al., 1994; Coale et al., 1996; Mackey et al., 2002; Kaupp et al., 2011). The EUC is an eastward-flowing subsurface current associated with upwellings that transports Fe from Papua New Guinea (PNG) toward South America along the equator (Gordon et al., 1997; Kaupp et al., 2011; Radic et al., 2011; Slemons et al., 2012; Winckler et al., 2016). Iron within the EUC is assumed to have both lithogenic and hydrothermal origins (Gordon et al., 1997). Specifically, the lithogenic component is suggested to primarily originate from rivers and sediments on the PNG continental margin (Mackey et al., 2002; Slemons et al., 2010; Radic et al., 2011; Labatut et al., 2014).

63 Although Fe concentration data are fundamental, isotopic measurements provide deeper
64 insight into both the provenance of Fe and internal processes governing its cycling (Lacan et
65 al., 2008; John et al., 2012; Conway and John, 2014; Ellwood et al., 2015). The isotopic
66 composition of Fe, expressed as $\delta^{56}\text{Fe}$ in per mil (‰), is defined as the deviation of the $^{56}\text{Fe}/^{54}\text{Fe}$
67 ratio of a sample from that of the IRMM-14 standard:

$$68 \quad \delta^{56}\text{Fe} = \frac{(^{56}\text{Fe}/^{54}\text{Fe})_{\text{sample}}}{(^{56}\text{Fe}/^{54}\text{Fe})_{\text{IRMM-14}}} - 1 \quad (\text{Equation 1})$$

69 The isotopic signatures can trace Fe from distinct sources, including fluvial inputs
70 (Fantle and DePaolo, 2004; Bergquist and Boyle, 2006; Ingri et al., 2006), sedimentary inputs
71 (Severmann et al., 2006; Homoky et al., 2009; Radic et al., 2011; Labatut et al., 2014),
72 hydrothermal inputs (Sharma et al., 2001; Severmann et al., 2004; Rouxel et al., 2008; Bennett
73 et al., 2009), and atmospheric inputs (Waeles et al., 2007; Flament et al., 2008; Kurisu et al.,
74 2016; Camin et al., 2025). They also provide information on internal oceanic processes.
75 Processes such as biological assimilation, dissolution, sorption, precipitation, complexation and
76 redox reactions, can modify the isotopic composition of Fe, through isotopic fractionation.

77 Despite advances, substantial uncertainties remain regarding both the isotopic signature
78 of sources and the isotopic fractionation of processes. Hydrothermal and sedimentary sources
79 are poorly characterized due to limited understanding of the processes governing Fe exchange
80 and speciation. Additionally, the extent and mechanisms of isotopic fractionation remain
81 incompletely understood. For example, fractionation caused by phytoplankton during
82 biological uptake remains uncertain, with studies suggesting preferential uptake of either lighter
83 or heavier isotopes (Lacan et al., 2008; Radic et al., 2011; Conway and John, 2014; Ellwood et
84 al., 2015, 2020; Klar et al., 2018; Sieber et al., 2021; Tian et al., 2023; John et al., 2024).

85 To better understand the sources, transport, and cycling of Fe in this region, the EUCFe
86 cruise (Equatorial Undercurrent Fe cruise) was conducted across the western and central
87 equatorial Pacific (RV Kilo Moana, PI: J. W. Murray, 2006). Iron isotope data from the EUCFe
88 cruise were previously published from four stations: three located in the west near PNG and
89 one in the open ocean (0° , 180°E) (Radic et al., 2011; Labatut et al., 2014). At the three stations
90 near PNG, an important source of dissolved Fe (DFe) was attributed to non-reductive exchange
91 processes between dissolved and mainly lithogenic particulate phases. The Fe isotope
92 signatures observed at the open ocean station indicated that in the deeper layer of the EUC the
93 Fe isotope signatures from the western Pacific were preserved toward the open ocean over more
94 than 4,000 km. The Fe isotopic composition of aerosols, collected during the cruise, was also
95 documented. Their slightly heavy signatures, $\delta^{56}\text{PFe} = +0.31 \pm 0.21$ ‰ (2SD, $n = 9$), were
96 interpreted as reflecting isotopic fractionation due to partial dissolution of crustal dust during
97 atmospheric transport (Camin et al., 2025).

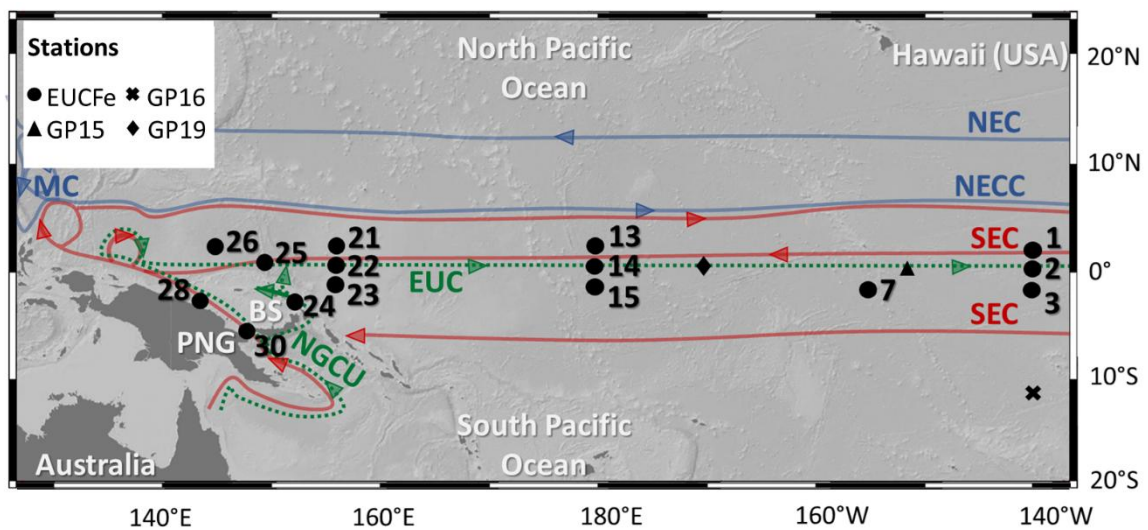
98 This present study reports Fe isotopic data from an additional 11 stations from the
99 EUCFe cruise in the equatorial band (2°N - 2°S) between Papua New Guinea and 140°W , over
100 more than 8,500 km along the equator and in the top 1 000 m of the water column. By expanding
101 the spatial coverage of concentration and isotopic measurements, we constrain the basin scale
102 Fe biogeochemical cycle in the western and central equatorial Pacific.

103

104 **2. HYDRODYNAMICAL CONTEXT, WATER MASSES AND CURRENTS**

105 Seawater samples ($n=76$) were collected during the EUCFe cruise from the surface to
106 1 000 m depth in the western and central equatorial Pacific Ocean. This area is influenced by
107 the South and the North Pacific subtropical gyres that shape the large-scale circulation. The
108 equatorial branches of those gyres are westward currents [extending from the surface to](#)

109 approximately 400 m depth (Cravatte et al., 2017): the North Equatorial Current (NEC) and the
 110 South Equatorial Current (SEC). The main surface and subsurface currents and the EUCFe
 111 stations with $\delta^{56}\text{Fe}$ data are represented in Figure 1.

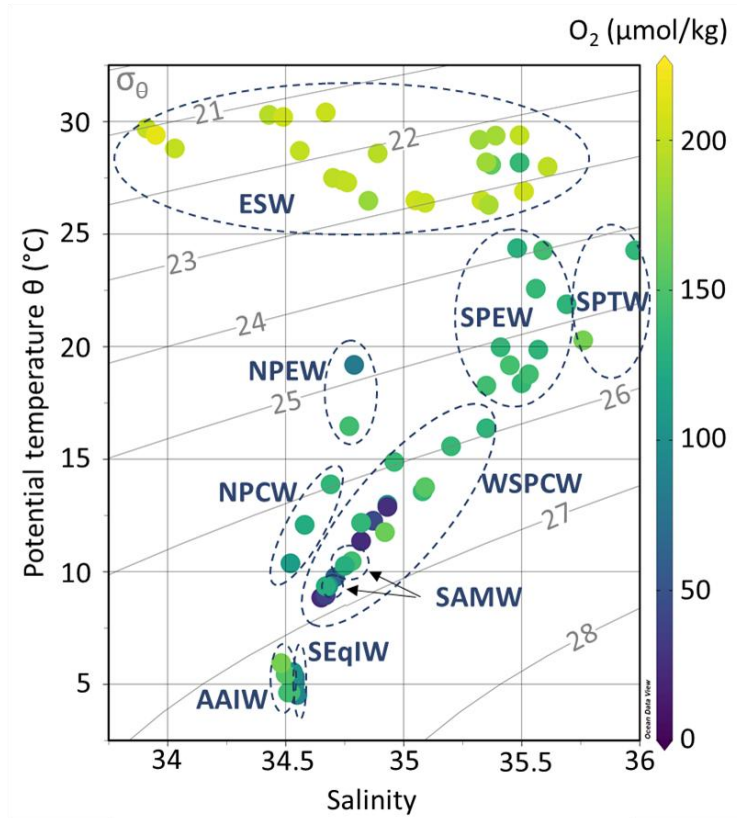


112
 113 Figure 1. Map of the EUCFe stations and some GP15, GP16 and GP19 stations. Main surface
 114 and subsurface currents are represented, in blue those carrying water masses of northern origins,
 115 in red those carrying waters of southern origins and in dashed green the undercurrents. BS:
 116 Bismarck Sea; EUC: Equatorial UnderCurrent; MC: Mindanao Current; NEC: North Equatorial
 117 Current; NECC: North Equatorial CounterCurrent; NGCU: New Guinea Coastal Undercurrent;
 118 SEC: South Equatorial Current (Delcroix et al, 1992; Fine et al, 1994; Kashino et al, 1996,
 119 2007; Johnson et al, 2002; Tomczak and Godfrey, 2003).

120 One of the specific structures of this circulation is the Equatorial Undercurrent (EUC).
 121 It is an intense subsurface equatorial current, with velocities up to $1 \text{ m}\cdot\text{s}^{-1}$ (Philander, 1973),
 122 flowing along the equator over 14,000 km (Tomczak and Godfrey, 2003). Its core rises toward
 123 the surface eastward, from an average depth of 200 m in the western equatorial Pacific, to depths
 124 of 130 m in the central equatorial Pacific and 40 m in the eastern equatorial Pacific (Tomczak
 125 and Godfrey, 2003; Talley et al., 2011). It is fed by waters from the Low-Latitude Western
 126 Boundary Currents (LLWBCs) composed at two-thirds by southern currents (New Guinea
 127 Coastal Current, New Guinea Coastal Undercurrent, New Ireland Coastal Undercurrent) and at
 128 one-third by northern currents (Mindanao Current) (Tsuchiya et al., 1989; Butt and Lindstrom,
 129 1994; Fine et al., 1994; Rodgers et al., 2003; Grenier et al., 2011). The EUC is therefore
 130 enriched with nutrients of continental origins and plays an essential role supplying the eastern
 131 equatorial Pacific HNLC area through the equatorial upwelling (Coale et al., 1996; Ryan et al.,
 132 2006; Slemmons et al., 2009; Kaupp et al., 2011).

133 Below the EUC, there is a westward subsurface flow, the Equatorial Intermediate Current
 134 (EIC). The EIC is bounded by eastward North and South Subsurface Countercurrents (NSCC
 135 and SSCC) centered around 2°N and 2°S , not shown in Figure 1 (Tomczak and Godfrey, 2003;
 136 Cravatte et al., 2017).

137



138

139 Figure 2. Potential temperature (θ , °C), salinity (S), dissolved oxygen concentrations (O_2 ,
 140 $\mu\text{mol.kg}^{-1}$) of EUCFe samples. Isopycnals are shown in gray lines (σ_θ , kg.m^{-3}). The dashed
 141 ellipses show water masses: Equatorial Surface Water (ESW), South Pacific Tropical Water
 142 (SPTW), South Pacific Equatorial Water (SPEW), North Pacific Equatorial Water (NPEW),
 143 Western South Pacific Central Water (WSPCW), North Pacific Central Water (NPCW), South
 144 Antarctic Mode Water (SAMW), South Equatorial Intermediate Water (SeqIW) and Antarctic
 145 Intermediate Water (AAIW).

146 Table 1. Water masses identified during the EUCFe cruise, with their characteristics in the study
 147 area: origin, depth, potential temperature (θ , °C), salinity, potential density anomaly (σ_θ , kg.m^{-3})
 148 and dissolved oxygen concentration (O_2 , $\mu\text{mol.kg}^{-1}$). Where the currents flow is specified.
 149 Currents acronym meanings are available in Figure 1, except for the North Equatorial
 150 Subsurface Current (NESC), the South Equatorial Subsurface Current (SESC) and the New
 151 Ireland Coastal Undercurrent (NICU).

152

Water Masses	Origin	EUCFe zone	Depth (m)	θ (°C)	Salinity	σ_{θ} (kg m ⁻³)	O ₂ (μ mol kg ⁻¹)	Currents	Characteristics	References
Equatorial Surface Water (ESW)	Mixing between the Tropical Surface Water and the Subtropical Surface Water, equatorial upwellings, advection of the Peru Current Water	Entire zone	0 - 100	21.0 - 30.5	33.5 - 35.7	20.5 - 23.5	108 - 193	SEC, NGCC, NICU, EUC	/	Fiedler & Talley, 2006; EUCFe sensor data
South Pacific Tropical Water (SPTW)	Subduction of surface waters in the tropics in a high-salinity area (evaporation excess) around the Polynesian region	Southeastern stations (stations 3 and 15)	100 - 200	18 - 25	35.7 - 36.7	24.3 - 25.3	134 - 167	SEC, NGCU, NGCC, NICU, EUC	Subsurface salinity maximum	Tsuchiya et al., 1989; Qu & Lindstrom, 2002; EUCFe sensor data
South Pacific Equatorial Water (SPEW)	Subduction of surface waters in the tropics in a high-salinity area (evaporation excess) around the Polynesian region: one branch, less salty, of the SPTW	Mainly western equatorial and southwestern stations	100 - 200	18 - 25	35.3 - 35.8	23.8 - 25.6	129 - 145	SEC, NICU, NGCU, NGCC, EUC	/	Tomczak & Hao, 1989; Tsuchiya et al., 1989; Qu & Lindstrom, 2002; Tomczak & Godfrey, 2003; EUCFe sensor data
North Pacific Equatorial Water (NPEW)	Mixture between SPEW and NPCW	Northern stations (stations 1 and 26)	100 - 200	16 - 20	34.7 - 35.0	24.3 - 25.5	80 - 145	NEC, EUC	Salinity minima of tropical waters	Tomczak & Godfrey, 2003; EUCFe sensor data
North Pacific Central Water (NPCW)	Northern subtropical front	Northwestern stations (stations 13, 21, 26)	200 - 300	10 - 17	33.5 - 34.7	25.2 - 26.4	110 - 135	EUC	Salinity minima of central waters	Emery & Meincke, 1986; Pickard & Emery, 1990; Tomczak & Godfrey, 2003; Grenier, 2012; EUCFe sensor data
Western South Pacific Central Water (WSPCW)	Subtropical convergence zone between Tasmania and New Zealand	Equatorial and southern stations and some northern stations	170 - 500	8.9 - 17	34.7 - 35.5	26.1 - 26.9	20 - 160	SEC, NGCU, NICU, EUC, EIC, NSCC, SSSC	Salinity maximum of central waters	Tsuchiya, 1981; Tomczak & Hao, 1989; Tsuchiya et al., 1989; Sokolov & Rintoul, 2000; Qu & Lindstrom, 2002; Tomczak & Godfrey, 2003; Qu et al., 2009; Grenier, 2012; EUCFe sensor data
South Antarctic Mode Water (SAMW)	Vertical convective overturning at the end of winter north of the Antarctic Circumpolar Current	Western stations (stations 22, 24, 25)	350 - 600	8.0 - 9.5	34.6 - 34.75	26.7 - 26.9	100 - 145	EIC, SEC	/	McCartney, 1977; Sokolov & Rintoul, 2000; EUCFe sensor data
South Equatorial Intermediate Water (SEqIW)	Mixing of AAIW and Pacific Deep Water	Every sample between 700 and 1000 m depth except the Southernmost stations close to the Bismarck Sea	700 - 1000	4.4 - 5.6	34.5 - 34.6	27.2 - 27.4	80 - 105	EIC, NSCC, SSSC, NESC, SESC	/	Wyrčki, 1962; Bingham & Lukas, 1995; Bostock et al., 2010; EUCFe sensor data
Antarctic Intermediate Water (AAIW)	Subduction of fresh surface water at the subantarctic front, west of the Drake Passage	Southernmost stations in the Bismarck Sea: at less than 60 km from Papua New Guinea coast (stations 24, 28, 30)	700 - 1000	4.7 - 6.0	34.4 - 34.6	27.2 - 27.3	140 - 170	SEC, NGCU, NGCC, NICU	Salinity minima of intermediate waters	Tsuchiya, 1991; Tsuchiya and Talley, 1996; Talley et al., 2011; EUCFe sensor data

154 In the equatorial Pacific Ocean between 140°E and 140°W, at least 9 different water
155 masses can be observed in the upper 1 000 m of the water column. Their θ , S and $[O_2]$
156 characteristics are shown in Figure 2 and reported in Table 1. The upper 100 m are mainly
157 composed of the Equatorial Surface Water (ESW), characterized by high temperatures and
158 oxygen concentrations. ESW is mainly formed from two water masses (Tropical Surface Water
159 (TSW) and Subtropical Surface Water (STSW)). Those are formed in the tropics where
160 evaporation exceeds precipitation and then transported toward the equator by the North and
161 South subtropical gyres. Due to mixing with upwelled waters, ESW is colder than TSW and
162 STSW (Fiedler and Talley, 2006). Between 100 and 200 m, there are three water masses, from
163 the saltiest to the freshest: the South Pacific Tropical Water (SPTW), the South Pacific
164 Equatorial Water (SPEW), the North Pacific Equatorial Water (NPEW) (Tsuchiya et al., 1989;
165 Lacan and Jeandel, 2001; Grenier et al., 2013). The SPTW originates from surface waters
166 subduction in the tropical South Pacific, a high-salinity area with excess evaporation (Tsuchiya
167 et al., 1989). The SPEW is a less salty version of the SPTW and the prevailing water mass
168 around the equator at these depths. It is the major constituent of the upper part of the EUC (σ_θ
169 $< 25.6 \text{ kg.m}^{-3}$) (Lacan and Jeandel, 2001; Tomczak and Godfrey, 2003; Grenier et al., 2011;
170 Grenier, 2012). The NPEW is formed by mixing of the SPEW and the North Pacific Central
171 Water (NPCW) (Tomczak and Godfrey, 2003). Between 200 and 500 m depth, central waters,
172 defined by a linear region on temperature-salinity diagrams, are found (Pollard et al., 1996;
173 Stramma and England, 1999; Tomczak and Godfrey, 2003). The Western South Pacific Central
174 Water (WSPCW), formed in the subtropical convergence zone between Tasmania and New
175 Zealand, is the major constituent of the lower part of the EUC ($\sigma_\theta > 25.6 \text{ kg.m}^{-3}$) (Tomczak and
176 Hao, 1989; Grenier et al., 2011; Grenier, 2012;). WSPCW is also the predominant water mass
177 at these depths in the study area. The North Pacific Central Water (NPCW) is formed in the
178 northern subtropical front (Tomczak and Godfrey, 2003). NPCW is found in the northern part
179 of the study area. Between 350 and 600 m, there is also the South Antarctic Mode Water
180 (SAMW), a water mass formed by vertical convective overturning at the end of the winter north
181 of the Antarctic Circumpolar Current (McCartney, 1977; Sokolov and Rintoul, 2000). The
182 SAMW is often associated with the Antarctic Intermediate Water (AAIW), a deeper water
183 mass. Both water masses, SAMW and AAIW, are found in the western part of the study area.
184 Between 600 and 1 000 m, two intermediate waters can be identified: the Equatorial
185 Intermediate Water (EqIW) and the AAIW. Some scientists refer to EqIW as part of the
186 Antarctic Intermediate Water (AAIW) (Yuan and Talley, 1992; Talley, 1999, 2008; Qu and
187 Lindstrom, 2004). In this article, the distinction between the EqIW and AAIW is relevant for
188 studying key parameters such as oxygen, nutrient concentrations and salinity along the equator.
189 The AAIW is formed by subduction of fresh surface water at the subantarctic front, west of the
190 Drake Passage (Tsuchiya, 1991; Talley et al., 2011). The EqIW is a mixing of AAIW and
191 Pacific Deep Water (formed without contact with the atmosphere by Antarctic Bottom Water,
192 Atlantic Deep Water and AAIW mixing) (Tomczak and Godfrey, 2003; Bostock et al., 2010).
193 It constitutes the predominant water mass at these depths in the study region.

194

195 3. SAMPLING AND ANALYTICAL PROCEDURES

196 Sampling and analytical procedures have been previously described (Radic et al., 2011;
197 Labatut et al., 2014). They are summarized below.

198 Seawater was sampled from surface to 1 000 m depth using acid cleaned Go-Flo bottles
199 (12 L) mounted on a trace metal rosette equipped with a CTD, lent by the University of Victoria
200 (Canada). Sample filtration was performed onboard in a homemade plastic room pressurized
201 with filtered air, with acid-cleaned Nuclepore™ membranes (0.4 μm pore size, 90 mm

202 diameter) housed in Teflon filter holders (Savillex™). After filtration, 10 liters of filtered
203 seawater were stored in acid-cleaned polyethylene containers and membranes were stored in
204 acid-cleaned Petri dishes.

205 Samples were processed and analyzed at the LEGOS laboratory (Observatoire Midi-
206 Pyrénées, Toulouse, France) between 2009 and 2012. All chemical procedures were conducted
207 in a trace-metal-clean laboratory under an ISO4 laminar flow hood, using high purity reagents
208 and acid cleaned labware.

209 Particles were fully digested in a mixture of 5 M HCl, 2.1 M HNO₃, and 0.6 M HF at
210 130 °C for 3 hours. To verify the completeness of the digestion, selected filters were re-digested,
211 confirming no particulate Fe (PFe) remained. Aliquots (2 %) were reserved for Al concentration
212 measurements using an Element-XR HR-ICP-MS. A ⁵⁷Fe-⁵⁸Fe double spike was added to the
213 remaining 98 % of the digested material and to filtered seawater, in preparation for isotopic
214 analyses. Dissolved iron was preconcentrated from filtered seawater on a NTA Superflow resin,
215 at pH = 1.8. Fe was purified from both types of samples with AG1-X4 anionic resin. Iron
216 isotopic compositions and concentrations were measured with a Neptune MC-ICP-MS.

217 Uncertainties are reported at a 95 % confidence level throughout this article. For Fe
218 concentrations and isotope measurements on the Neptune, the total procedural recovery was
219 93 ± 25 % for PFe and 86 ± 33 % for DFe. The total procedural blanks were 0.74 ± 1.17 ng
220 (2SD) for DFe and 7.47 ± 1.09 ng (2SD) for PFe. This amounts to 0.5 % and 0.6 % of the
221 samples average Fe content for DFe and PFe, respectively and 2.8% and 9.7 % for the sample
222 with the smallest Fe content for DFe and PFe, respectively. For DFe, the filtered seawater from
223 a sample was divided into several aliquots, then each was processed individually (including
224 different double spiking, preconcentration and purification). For PFe, each sample, i.e.,
225 membrane, was first digested (no division of the membrane before digestion), then the digested
226 sample was divided into several aliquots, and each was processed individually (including
227 different double spiking and purification). In some instances, duplicate samples are taken at
228 sea, from the same cast. These replicates are termed "Go-Flo replicates" in the Table A1.
229 Repeatability was 8 % for DFe concentrations, 4 % for PFe concentrations, 0.05 ‰ for δ^{56} DFe
230 and 0.04 ‰ for δ^{56} PFe. This level of precision is better than the long-term external precision of
231 0.07 ‰, determined from repeated analyses of an in-house "ETH Hematite" isotopic standard.
232 As a result, uncertainties for δ^{56} Fe data are reported as either ± 0.07 ‰ or the internal
233 measurement uncertainty (2 standard errors), whichever is larger.

234 The LEGOS Fe isotope protocol has been validated through intercalibration and
235 intercomparison exercises (Boyle et al., 2012; Conway et al., 2016) and detailed in Lacan et al.
236 (2008, 2010, 2021). Accuracy (referring to the two concepts of trueness and precision) of
237 elemental concentrations measured by HR-ICP-MS was regularly verified using the certified
238 SLRS-5 river water material and through intercalibration exercises (Yeghicheyan et al., 2013,
239 2019).

240

241 4. RESULTS

242 Concentrations and isotopic compositions of DFe and PFe in seawater are reported in
243 Table 2. Previously published data from four stations (14, 24, 28 and 30) are included here for
244 clarity (Radic et al., 2011; Labatut et al., 2014). All Fe concentrations, Fe isotopic compositions,
245 temperature, salinity, oxygen data and an intercalibration report, have been included in the
246 GEOTRACES Data Product. They are also available on the SEANOE open data repository
247 (Lacan et al., 2025).

248 Table 2. Location, depth, hydrological properties, concentration and isotopic composition of
 249 dissolved and particulate Fe (DFe and PFe). Concentration relative uncertainties are 8.0 % for
 250 DFe and 4.3 % for PFe (95% confidence level). U95 stands for measurement uncertainty at the
 251 95 % confidence level. For most samples, dissolved O₂ concentration was measured in the
 252 samples onboard. When direct measurements were not available, as indicated by the (*) symbol,
 253 oxygen concentrations from the oxygen sensor on the rosette were used following calibration
 254 with in situ data. The (+) and (°) symbols indicate data previously published by Radic et al.
 255 (2011) and Labatut et al. (2014), respectively. ESW: Equatorial Surface Water; SPTW: South
 256 Pacific Tropical Water; SPEW: South Pacific Equatorial Water; NPEW: North Pacific
 257 Equatorial Water; NPCW: North Pacific Central Water; WSPCW: Western South Pacific
 258 Central Water; SAMW: South Antarctic Mode Water; SEqIW: South Equatorial Intermediate
 259 Water; AAIW: Antarctic Intermediate Water; Chloro. Max: Chlorophyll Maximum layer.

260

GoFlo bottle	Depth (m)	θ (°C)	Salinity	O ₂ (μmol. kg ⁻¹)	σ _θ (kg. m ⁻³)	Water mass	DFe (nmol. kg ⁻¹)	δ ⁵⁶ DFe (‰)	δ ⁵⁶ DFe U95 (‰)	PFe (nmol. kg ⁻¹)	δ ⁵⁶ PFe (‰)	δ ⁵⁶ PFe U95 (‰)
STATION 1 (1.6°N 140.0°W, cast TM3, 25 August 2006, bottom depth: 4364 m)												
12	15	26.5	35.05	204	22.93	ESW	0.26	+0.43	0.08	0.39	+0.06	0.07
10	48	26.4	35.09	202	22.98	ESW (Chloro. Max.)	0.26	+0.32	0.07	0.43	+0.25	0.07
8	119	19.2	34.79	81	24.82	NPEW	0.37	+0.28	0.08	0.24	+0.23	0.07
6	268	12.3	34.87	43	26.43	WSPCW	0.36	-0.19	0.11	0.21	+0.06	0.07
4	497	8.8	34.65	(°) 23	26.88	WSPCW	0.71	-0.22	0.09	0.38	+0.12	0.07
2	794	5.3	34.54	(°) 87	27.28	SEqIW	0.77	+0.40	0.07	0.30	-0.11	0.07
STATION 2 (0.0°N 140.0°W, cast TM9, 26 August 2006, bottom depth: 4333 m)												
12	15	26.5	35.33	201	23.13	ESW	0.13	+0.19	0.07	0.47	+0.19	0.07
10	49	26.2	35.36	188	23.23	ESW (Chloro. Max.)	0.38	+0.14	0.09	—	—	—
8	114	24.3	35.59	143	24.00	SPEW	0.17	+0.25	0.07	—	—	—
6	246	13.0	34.93	98	26.34	WSPCW	0.44	+0.29	0.07	—	—	—
4	348	11.4	34.82	(°) 24	26.57	WSPCW	0.43	-0.10	0.07	—	—	—
2	992	4.6	34.55	(°) 86	27.37	SEqIW	0.61	+0.11	0.07	—	—	—
STATION 3 (2.0°S 139.6°W, cast TM11, 27 August 2006, bottom depth: 4257 m)												
12	13	26.9	35.51	203	23.13	ESW	0.07	—	—	0.60	+0.41	0.07
10	59	26.9	35.51	205	23.14	ESW (Chloro. Max.)	0.06	+0.31	0.07	—	—	—
8	110	20.3	35.76	167	25.25	SPTW	0.14	+0.30	0.12	0.14	+0.33	0.07
7	198	12.8	34.93	25	26.37	WSPCW	0.24	-0.06	0.07	—	—	—
4	476	9.0	34.67	(°) 36	26.87	SEqIW	0.43	+0.14	0.07	—	—	—
1-2	993	4.5	34.55	(°) 91	27.37	SEqIW	0.41	+0.35	0.07	0.40	+0.15	0.08
STATION 7 (2.1°S 155.1°W, cast TM16, 02 September 2006, bottom depth: 4992 m)												
11	75	27.9	35.61	196	22.87	ESW (Chloro. Max.)	0.07	—	—	0.55	+0.22	0.07
STATION 13 (2.0°N 179.6°W, cast TM25, 10 September 2006, bottom depth: 5218 m)												

12	15	30.3	34.43	195	21.20	ESW	0.07	+0.79	0.07	0.80	-0.04	0.08
10	79	29.2	35.32	184	22.23	ESW (Chloro. Max.)	0.10	+0.35	0.07	0.49	+0.26	0.11
8	119	28.2	35.49	137	22.69	ESW	0.07	+0.72	0.07	—	—	—
7	170	13.8	34.69	134	25.98	NPCW	0.32	+0.30	0.08	0.87	+0.12	0.10
4	377	10.3	34.75	(*) 68	26.70	WSPCW	0.47	+0.35	0.07	1.02	+0.12	0.12
2	892	5.1	34.54	97	27.30	SEqIW	0.41	+0.25	0.07	0.31	—	—

STATION 14 (0.0°N 180°E, cast TM28, 11 September 2006, bottom depth: 5260 m) (+)

12	14	30.4	34.67	201	21.35	ESW	0.06	—	—	0.37	+0.27	0.07
10	98	29.4	35.39	186	22.22	ESW (Chloro. Max.)	0.06	+0.58	0.07	0.43	+0.43	0.09
8	139	22.6	35.56	137	24.48	SPEW	0.20	+0.31	0.08	0.53	+0.13	0.09
6	197	14.9	34.86	140	25.88	WSPCW	0.53	+0.40	0.12	0.53	+0.40	0.07
4	397	9.8	34.71	64	26.76	WSPCW	0.61	+0.01	0.07	0.81	+0.15	0.11
2	842	5.3	34.54	82	27.27	SEqIW	0.59	+0.22	0.08	0.51	+0.28	0.10

STATION 15 (2.0°S 180.0°E, cast TM30, 12 September 2006, bottom depth: 5390 m)

12	16	30.2	34.49	206	21.27	ESW	0.06	+0.55	0.07	0.39	+0.27	0.07
10	75	29.3	35.49	199	22.32	ESW (Chloro. Max.)	0.05	—	—	0.27	+0.30	0.07
8	139	24.2	35.98	134	24.31	SPTW	0.10	+0.43	0.07	0.33	+0.23	0.12
6	171	16.4	35.35	133	25.93	WSPCW	0.23	+0.20	0.07	0.49	+0.12	0.11
2	844	5.3	34.53	99	27.27	SEqIW	0.58	+0.32	0.07	0.98	-0.05	0.10

STATION 21 (2.0°N 156.0°E, cast TM40, 20 September 2006, bottom depth: 2587 m)

10	75	28.1	35.37	158	22.65	ESW (Chloro. Max.)	0.11	—	—	0.41	+0.18	0.14
8	147	24.4	35.48	129	23.89	SPEW	0.36	+0.40	0.08	0.60	-0.05	0.07
7	194	12.0	34.58	124	26.25	NPCW	0.45	+0.16	0.07	1.59	+0.05	0.07

STATION 22 (0.2°N 156.0°E, cast TM43, 21 September 2006, bottom depth: 2049 m)

12	24	29.7	33.91	200	21.00	ESW	0.09	—	—	0.39	+0.19	0.07
10	54	28.6	34.89	195	22.12	ESW (Chloro. Max.)	0.09	—	—	0.32	+0.22	0.07
8	191	18.2	35.35	143	25.49	SPEW	0.71	+0.48	0.08	2.89	+0.00	0.07
6	257	12.2	34.82	134	26.41	WSPCW	0.96	+0.40	0.07	4.26	+0.02	0.07
4	393	9.3	34.68	(*) 101	26.82	SAMW	—	—	—	1.51	+0.01	0.12
3	393	9.3	34.68	(*) 101	26.82	SAMW	0.91	+0.25	0.07	1.68	+0.05	0.15

STATION 23 (1.2°S 155.6°E, cast TM45, 22 September 2006, bottom depth: 1997 m)

10	74	28.2	35.35	(*) 183	22.60	ESW (Chloro. Max.)	0.07	+0.26	0.09	0.29	+0.14	0.11
8	185	18.4	35.50	(*) 138	25.56	SPEW	0.46	+0.32	0.09	1.83	-0.03	0.14
6	218	13.6	35.08	(*) 137	26.34	WSPCW	0.72	+0.29	0.07	1.87	+0.04	0.07
5	218	13.6	35.08	(*) 137	26.34	WSPCW	0.72	+0.30	0.11	2.52	-0.01	0.13
4	218	13.6	35.08	(*) 137	26.34	WSPCW	0.75	+0.22	0.07	2.70	+0.03	0.12

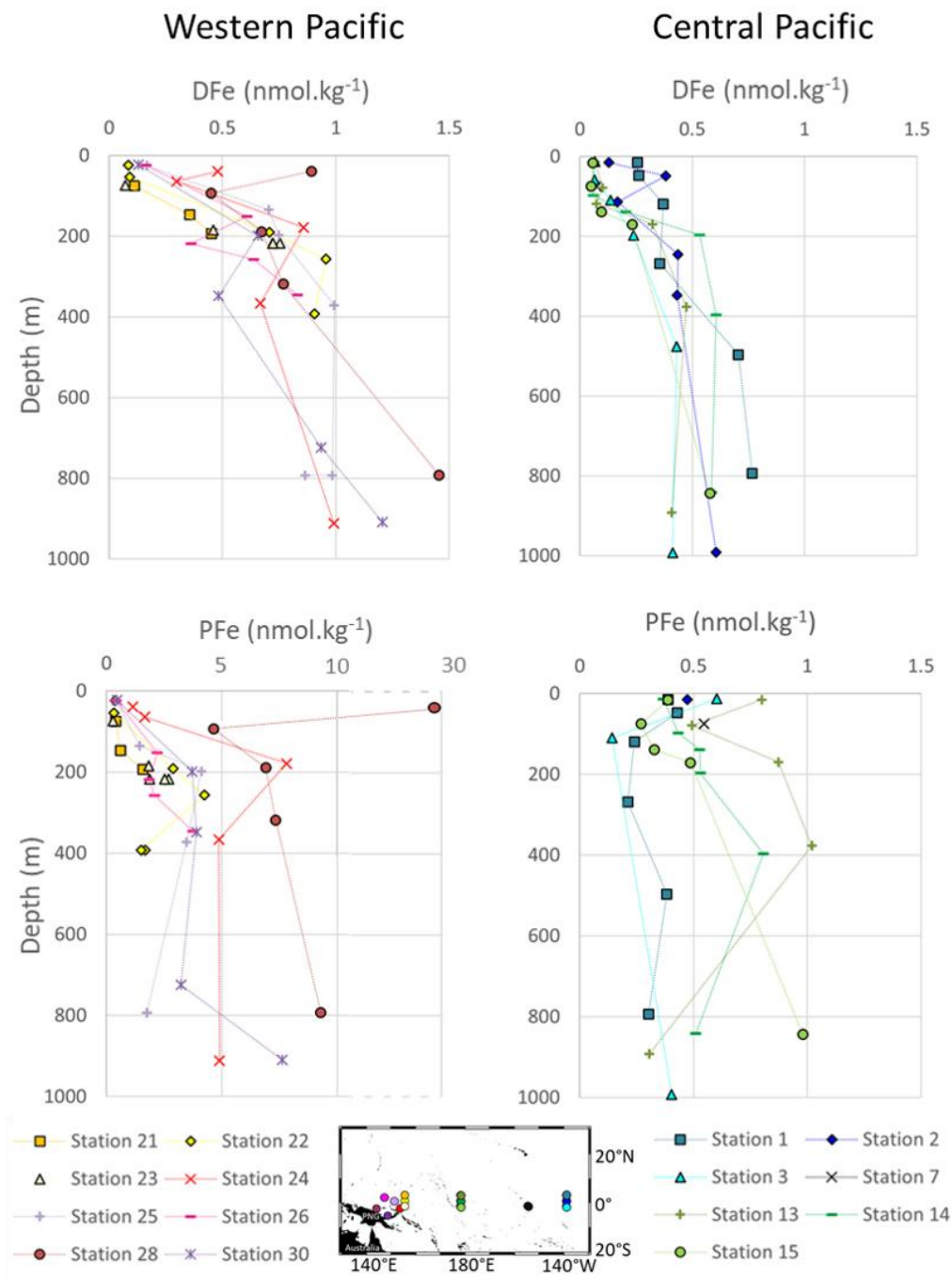
STATION 24 (3.2°S 152.3°E, cast TM47, 23 September 2006, bottom depth: 1669 m) (°)

11	39	28.7	34.56	199	21.83	ESW	0.48	-0.03	0.07	1.15	+0.13	0.14
----	----	------	-------	-----	-------	-----	------	-------	------	------	-------	------

9	64	27.4	34.74	196	22.38	ESW (Chloro. Max.)	0.30	+0.20	0.07	1.66	+0.01	0.16
7	179	19.9	35.57	133	25.22	SPEW	0.86	-0.03	0.07	7.81	-0.48	0.11
5	367	10.5	34.78	(*) 143	26.70	WSPCW	0.67	+0.27	0.08	4.87	-0.03	0.12
2	912	4.6	34.52	141	27.34	AAIW	0.99	+0.34	0.07	4.91	+0.00	0.10
STATION 25 (0°N 149.3°E, cast TM50, 25 September 2006, bottom depth: 3364 m)												
11	25	29.4	33.95	215	21.14	ESW	0.17	—	—	0.44	+0.25	0.09
9	135	21.9	35.69	133	24.79	SPEW	0.70	+0.03	0.13	1.44	-0.52	0.10
6	198	15.6	35.20	136	26.00	WSPCW	0.75	+0.38	0.14	4.12	+0.02	0.07
5	372	10.3	34.75	(*) 126	26.71	SAMW	0.99	—	—	3.48	+0.00	0.07
3	793	5.5	34.53	(*) 103	27.24	SEqIW	0.98	+0.13	0.07	1.76	-0.06	0.07
2	793	5.5	34.53	(*) 103	27.24	SEqIW	0.87	—	—	1.77	-0.05	0.07
STATION 26 (1.6°N 145.0°E, cast TM52, 26 September 2006, bottom depth: 4490 m)												
11	24	28.8	34.03	200	21.40	ESW	0.16	—	—	0.42	—	—
8	152	20.0	35.41	135	25.08	SPEW	0.61	—	—	2.20	+0.01	0.07
6	219	16.4	34.77	(*) 144	25.48	NPEW	0.36	—	—	1.85	+0.12	0.07
5	258	10.4	34.52	(*) 111	26.51	NPCW	0.64	+0.20	0.07	2.09	+0.04	0.07
3	346	9.4	34.67	(*) 127	26.79	WSPCW	0.83	—	—	3.76	+0.02	0.07
STATION 28 (3.4°S 143.9°E, cast TM56, 28 September 2006, bottom depth: 2256 m) (+) (°)												
10	39	27.5	34.70	196.6	22.32	ESW	0.89	+0.53	0.07	29.45	+0.04	0.09
8	94	26.5	34.85	180.9	22.77	ESW (Chloro. Max.)	0.45	+0.40	0.10	4.64	+0.01	0.07
7	189	19.1	35.45	145	25.33	SPEW	0.67	+0.43	0.11	6.91	+0.29	0.07
5	319	13.8	35.09	154	26.31	WSPCW	0.77	+0.29	0.07	7.34	+0.04	0.07
2	793	5.5	34.50	151	27.22	AAIW	1.46	+0.06	0.07	9.29	-0.03	0.10
STATION 30 (5.6°S 147.4°E, cast TM61, 30 September 2006, bottom depth: 1040 m) (°)												
10	23	27.3	34.76	(*) 200	22.44	ESW	0.13	—	—	0.45	+0.30	0.11
7	199	18.7	35.53	(*) 144	25.49	SPEW	0.65	+0.41	0.12	3.72	+0.17	0.07
6	348	11.8	34.92	(*) 162	26.57	WSPCW	0.48	+0.31	0.07	3.90	+0.20	0.07
3	724	5.9	34.48	(*) 166	27.15	AAIW	0.94	+0.44	0.12	3.23	+0.01	0.07
2	909	4.6	34.51	(*) 143	27.33	AAIW	1.21	—	—	7.62	-0.03	0.07

261

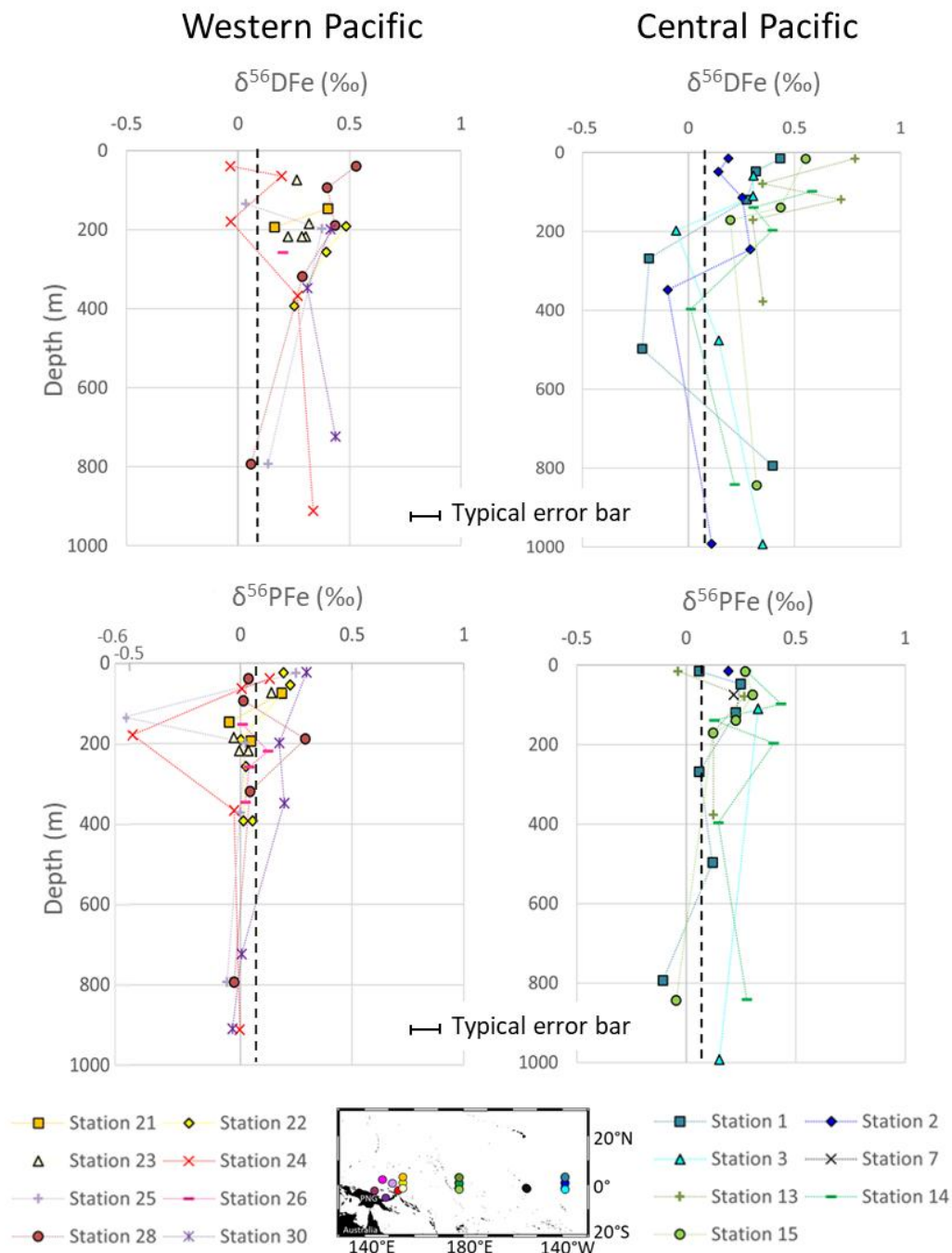
262 Two distinct groups of stations emerge from these observations. These are the western
263 equatorial Pacific and central equatorial Pacific. In the western equatorial Pacific, PFe
264 concentrations were significantly higher, approximately seven times larger, than typical open
265 ocean values. This group includes stations 21, 22, 23, 24, 25, 26, 28 and 30. In the central
266 equatorial Pacific, PFe concentrations were mostly typical of open ocean values. This group
267 includes stations 1, 2, 3, 7, 13, 14 and 15. Data for both areas are shown in Figures 3 and 4.



268

269 Figure 3. Profiles of concentrations of DFe and PFe in nmol.kg⁻¹ in the western equatorial and
 270 central equatorial Pacific. For each station, the error bars are smaller than the symbols for Fe
 271 concentrations: on average 8 % for DFe and 4 % for PFe. Stations 14 and 28 were previously
 272 published by Radic et al. (2011) and stations 24, 28 and 30 by Labatut et al. (2014). The x-axis
 273 is broken to show all PFe concentrations from western equatorial Pacific stations.

274



275

276 Figure 4. $\delta^{56}\text{DFe}$ and $\delta^{56}\text{PFe}$ profiles in the western equatorial and central equatorial Pacific.
 277 The black dashed line indicates the crustal value, +0.07 ‰ (Poitrasson, 2006). Individual error
 278 bars are not shown for clarity, but typical uncertainty (± 0.07 ‰) is indicated by the scale bar.

279

280 4.1. IRON CONCENTRATIONS

281 DFe and PFe concentrations ranged from 0.05 to 1.46 nmol.kg^{-1} and from 0.14 to 29.45
 282 nmol.kg^{-1} , respectively.

283 A few common features in Fe concentration profiles can be identified across stations
 284 from the surface to 1 000 m. i) With the exception of station 28 located near the mouth of the
 285 Sepik River, lowest concentrations were found near the surface, mostly in the chlorophyll

286 maximum layer, where biological uptake depletes the concentration of bioavailable Fe. ii) From
287 the surface to 200 m depth, Fe concentrations tended to increase. Deeper than 200 m, the
288 profiles became more variable, with no uniform trend across stations. iii) Stations 3, 13, 14 and
289 15 displayed typical open ocean, nutrient like, DFe profiles. iv) The particulate iron (PFe)
290 fraction predominated over the dissolved fraction (DFe), accounting on average for 80 %
291 mol.mol^{-1} of total iron (TFe) at western equatorial Pacific stations (140°E–156°E) and 66 %
292 mol.mol^{-1} at central equatorial Pacific stations (180°E–140°W) (Figure A1).

293 Slemons et al. (2010, 2012) measured DFe and PFe concentrations by FIA during the
294 same cruise. All data were of the same order of magnitude and ranged similarly. However, our
295 data were almost systematically slightly lower (with a mean difference of $0.35 \pm 0.44 \text{ nmol.kg}^{-1}$
296 1 for DFe and $0.35 \pm 0.90 \text{ nmol.kg}^{-1}$ for PFe). In addition, EUCFe DFe and PFe concentration
297 data are in good agreement with data published in the same area (John et al., 2018; Marsay et
298 al., 2018b; Zheng and Sohrin, 2019; Cohen et al., 2021; Sarthou et al., 2025).

299

300 4.2. IRON ISOTOPIC COMPOSITIONS

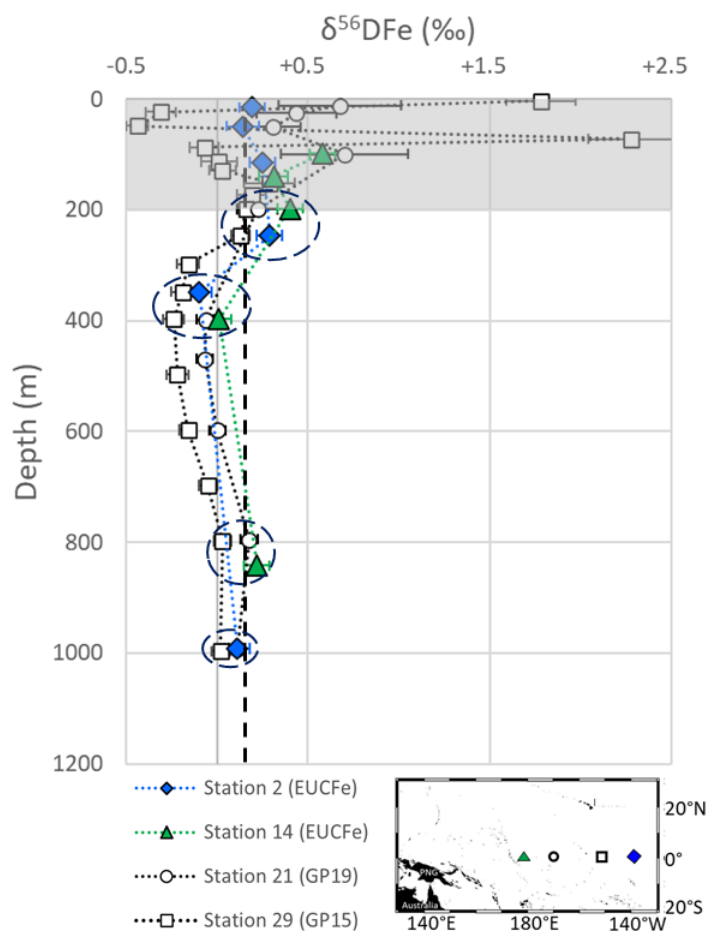
301 The isotopic signatures of dissolved ($\delta^{56}\text{DFe}$) and particulate Fe ($\delta^{56}\text{PFe}$) ranged
302 from -0.22 to +0.79 ‰ and -0.52 to +0.43 ‰, respectively (Figure 4).

303 Across all stations, 85 % of the samples had isotopic compositions of dissolved iron
304 ($\delta^{56}\text{DFe}$) higher than the upper continental crust (UCC) reference value of +0.07 ‰ (Poitrasson,
305 2006). $\delta^{56}\text{DFe}$ of western equatorial Pacific stations ranged from -0.03 ‰ to +0.53 ‰, with an
306 average of $+0.28 \pm 0.30 \text{ ‰}$ (2SD, n=27) and showed no systematic variation with depth or
307 location. At the central equatorial Pacific stations, $\delta^{56}\text{DFe}$ ranged from -0.22 ‰ to +0.79 ‰,
308 with an average of $+0.27 \pm 0.45 \text{ ‰}$ (2SD, n=32). The surface layer exhibited relatively heavy
309 isotopic signatures (around +0.5 ‰), which generally decreased with depth, reaching values
310 around -0.2 ‰ at approximately 400 m. Below this depth, between 800 and 1 000 m, $\delta^{56}\text{DFe}$
311 values increased again, to +0.4 ‰.

312 The isotopic compositions of particulate iron ($\delta^{56}\text{PFe}$) at the western equatorial Pacific
313 stations, $+0.03 \pm 0.32 \text{ ‰}$ (2SD, n=39) on average, were remarkably homogeneous and
314 remained close to the UCC value, except for two samples from stations 24 and 25. At the central
315 equatorial Pacific stations, $\delta^{56}\text{PFe}$ were slightly more variable, from -0.11 to +0.43 ‰ (with an
316 average of $+0.19 \pm 0.27 \text{ ‰}$, 2SD, n=26), and 81 % of the samples were heavier relative to the
317 UCC.

318 EUCFe data can be compared with three nearby cruises: GEOTRACES GP16 (2013), a
319 zonal cruise along 10°S, from 75°W to 155°W, GEOTRACES GP15 (2018), a meridional
320 section along 150°W with one station located at the equator and GEOTRACES GP19 (2015),
321 a meridional section along 170°W with one station located at the equator (Figure 1). In the
322 equatorial Pacific area, the circulation is highly zonal, and previous studies have shown that the
323 water mass geochemistry at 12°S is not directly linked to that of the equatorial band (Lacan and
324 Jeandel, 2001). This prevents the use of GP16 data and limits that of GP15 and GP19 to their
325 equatorial stations (stations 29 and 21, respectively). These GP15 and GP19 Fe isotope data
326 have not yet been published but are available in GEOTRACES Intermediate Data Product 2025
327 (GEOTRACES Intermediate Data Product Group, 2025). Figure 5 displays the GP15 station 29
328 and GP19 station 21 $\delta^{56}\text{DFe}$ profiles with the closest equatorial EUCFe stations, stations 2 and
329 14 (EUCFe station 7 is excluded from this comparison because it only reports a single data
330 point at 75 m). Given the nine year lag between the two cruises, and the thousand km between
331 the stations, the upper 200 m are excluded from this comparison due to potential variabilities.

332 At four depths, approximately 200, 400, 800 and 1 000 m, $\delta^{56}\text{DFe}$ data from the **three** cruises
333 can be compared (Figure 5). These are in excellent agreement. No $\delta^{56}\text{PFe}$ data have been
334 reported for **GP15** and **GP19**.



335
336 Figure 5. Comparison of $\delta^{56}\text{DFe}$ values from the EUCFe, **GP15** and **GP19** cruises. The upper
337 200 m, shaded in gray, are excluded from the comparison. The dashed ellipses show the 4
338 depths where comparison can be made for $\delta^{56}\text{DFe}$ values. **Please note that at 1 000 m, values**
339 **from stations 2, 21 and 29 are close, making station 21 less visible.** The black dashed line
340 indicates the crustal value. **The GP15 cruise data were produced by M. Sieber and T. Conway,**
341 **and the GP19 cruise data were produced by T. Conway, M. Sieber, and D. Vance; both datasets**
342 **are available in the GEOTRACES Data product (GEOTRACES Intermediate Data Product**
343 **Group, 2025).**

344 345 **5. DISCUSSION**

346 347 **5.1. INFLUENCE OF EXTERNAL IRON INPUTS IN THE WESTERN EQUATORIAL PACIFIC**

348 Fe concentrations **throughout the entire water column in the western equatorial Pacific**
349 **were approximately twice as high for DFe ($0.63 \text{ nmol.kg}^{-1}$ compared to $0.30 \text{ nmol.kg}^{-1}$, on**
350 **average) and approximately seven times higher for PFe ($3.58 \text{ nmol.kg}^{-1}$ compared to 0.49**
351 **nmol.kg^{-1} , on average) relative to the central equatorial Pacific stations. The particulate Fe (PFe)**
352 **fraction dominated total Fe (TFe), particularly in the western equatorial Pacific stations, where**

353 PFe/TFe ratios ranged from 63 to 97 % mol.mol⁻¹ (Figure A1). These patterns were documented
354 previously in several studies, and attributed to lithogenic inputs from terrestrial sources, with
355 occasional hydrothermal contributions and minimal input from atmospheric sources (Milliman,
356 1995; Kineke et al., 2000; Mackey et al., 2002; Slemmons et al., 2010; Radic et al., 2011; Labatut
357 et al., 2014).

358 A box model (Figure 6) for the region defined by (133°E–177°W, 9°S–15°N) was used
359 to investigate the relative importance of possible PFe sources leading to these high
360 concentrations. The model includes PFe transported by oceanic currents, atmospheric
361 deposition and delivered by rivers (notably the Sepik River, with potential deposition to and
362 resuspension from sediments). Particle settling within the water column and hydrothermal
363 sources were neglected.

364 The transport of water masses in this area, from the surface to a depth of 1 000 m, was estimated
365 at 19.4 ± 0.4 Sv (1SD), based on the flow in Vitiaz Strait during the Austral winter (i.e., the
366 same period as the EUCFe cruise) (Germineaud et al., 2016). The incoming water is assumed
367 to carry a typical open ocean PFe concentration (average value for the upper 1 000 m of the
368 water column, station 36, GP16 cruise) of 0.15 ± 0.08 nmol.kg⁻¹ (1SD) (Marsay et al., 2018),
369 prior to enrichment within the study area. The flux of PFe transported by water masses into this
370 area, calculated as the product of these two quantities, is $\text{Flux PFe}_{\text{SW in}} = 14.5 \times 10^6$ g(PFe).day⁻¹.
371 The average PFe concentration in this area (stations 21 to 30) ranged between 2.9 and 3.8
372 nmol.kg⁻¹ depending on the calculation method chosen (Table A1). The fluxes derived from
373 these concentrations will be given as a range. This leads to a PFe flux transported out of the
374 area by water masses, $\text{Flux PFe}_{\text{SW out}}$, between 272×10^6 and 357×10^6 g(PFe).day⁻¹
375 (concentration multiplied by 19.4 Sv). In a steady state model, where inputs are balanced by
376 outputs, one or more sources must be contributing approximately between 258×10^6 and
377 342×10^6 g(PFe).day⁻¹ to this area.

378 Particulate iron atmospheric deposition was estimated using the Fe concentration in aerosols
379 over this region, measured during the same cruise at 3.01 ng.m⁻³ (Camin et al., 2025), multiplied
380 by a bulk aerosol deposition velocity. The deposition area shown in Figure 6, chosen as
381 representative of this region of elevated PFe concentrations, covers approximately 1.54×10^7
382 km² (the box model surface area of 1.6×10^7 km² minus the New Guinea land area of
383 0.08×10^7 km²; Baldacchino et al., 2024). The bulk aerosol deposition velocity, denoted V_b
384 (m.day⁻¹), includes both wet and dry deposition. It can be calculated from the precipitation rate
385 (mm.day⁻¹) according to the formula from Kadko et al., 2020, recently updated by He et al.,
386 2025, who used ⁷Be as a proxy for atmospheric deposition:

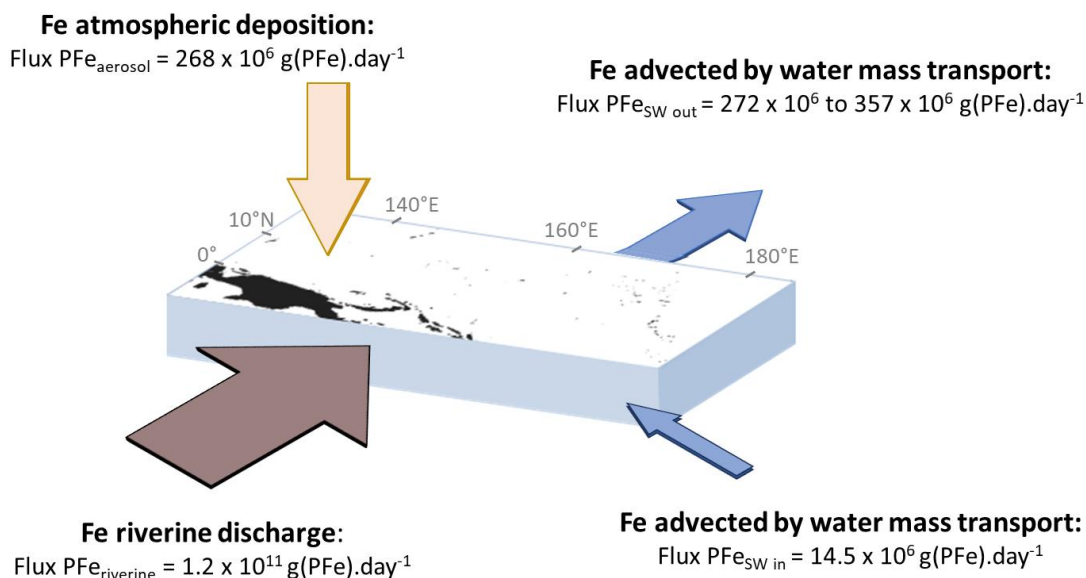
387
$$V_b = 413 \pm 22 \times \text{Precipitation Rate} + 1069 \pm 71 \quad (\text{Equation 2})$$

388 To estimate the precipitation rate, we used the NASA Giovanni data product TRMM to
389 determine the mean daily precipitation rate over the entire region considered in the box model
390 from September 20 to 30, 2006. The mean value was 11.4 ± 6.6 mm.day⁻¹ (2SD) (Table A2).
391 Applying Equation 2, the bulk aerosol deposition velocity is therefore 5 777 m.day⁻¹. The
392 resulting atmospheric PFe deposition flux was $\text{Flux PFe}_{\text{aerosol}} = 268 \times 10^6$ g(PFe).day⁻¹. This
393 estimate accounts for between 78 and 104 % of the required external sources (Table A1).
394 However as discussed below, this PFe atmospheric deposition flux is orders of magnitudes
395 lower than that delivered by rivers.

396 Papua New Guinea accounts for 8 to 10 % of the global export of sediment to the ocean ($1.7 \times$
397 10^{17} g(sediment).year⁻¹) (Milliman et al., 1999). The Sepik River and other northern rivers of
398 PNG discharge 8.6×10^{14} g(sediment).year⁻¹ to this study area (Milliman et al., 1999).
399 Assuming that Fe amounts to 5 % w.w⁻¹ of the sediment discharge, (the UCC value from
400 Rudnick and Gao, 2014), the estimated riverine discharge of PFe to the western equatorial

401 Pacific is $4.3 \times 10^{13} \text{ g(PFe).year}^{-1}$, i.e., $1.2 \times 10^{11} \text{ g(PFe).day}^{-1}$. This estimate accounts for
402 between 35 064 and 46 556 % of the required external sources (Table A1).

403 Thus, the riverine PFe flux is 448-fold larger than the atmospheric PFe flux. This flux
404 comparison argues in favor of a contribution dominated by input from rivers. Isotopic signatures
405 provide an additional constraint and also support a riverine source, as the $\delta^{56}\text{PFe}$ values are
406 close to crustal values in this region (Table 2 and Figure 4), whereas aerosols exhibit a heavier
407 isotopic signature, around +0.3 ‰ (Camin et al., 2025).



408
409 Figure 6. Box model describing PFe inputs and output to the western equatorial Pacific region.
410 Note that all of the external sources end up in seawater. Some are removed to the sediments.

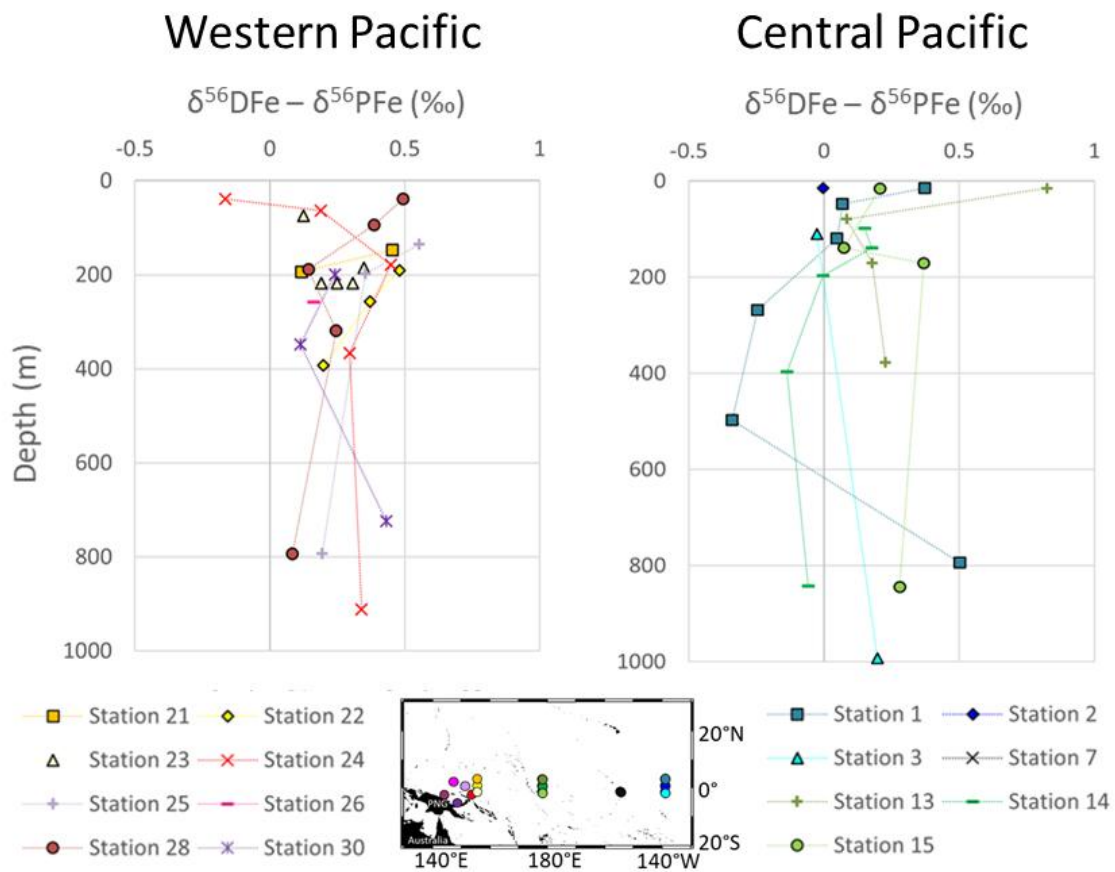
411 Regarding riverine particles, the question of their transport mechanism over such a
412 distance from the coast (~1 200 km) arises. The Sepik River and other northern rivers of PNG
413 deliver large sediment loads to the coastal ocean due to factors including intense rainfall from
414 the Inter-Tropical Convergence Zone, a narrow shelf associated with the active margin, the
415 sediment erodibility (geology, human activities) and tectonism (seismic and volcanic activity,
416 relief) (Milliman and Syvitski, 1992). Lithogenic iron (Fe) observed at the western equatorial
417 Pacific stations can be due to direct fluvial inputs, resuspended sediments, isopycnal plumes,
418 and hyperpycnal flows (Kineke et al., 2000; Mackey et al., 2002; Kuehl et al., 2004; Renagi et
419 al., 2010; Slemmons et al., 2012). These processes can transport Fe seaward across the slope
420 (Kineke et al., 2000; Kuehl et al., 2004; Renagi et al., 2010). These lithogenic inputs, leading
421 to very significant PFe excess compared to open ocean values, extend throughout the sampled
422 water column (0 – 1 000 m) at all stations in the western equatorial Pacific. Therefore, we
423 discuss these data below as a whole, without distinguishing between different water masses or
424 currents.

425 At the western equatorial Pacific stations, PFe isotopic compositions are close to the
426 UCC reference value, supporting a predominantly lithogenic origin discussed above (Table 2
427 and Figure 4). Only two samples, from stations 24 and 25, exhibit near-zero $\delta^{56}\text{DFe}$ and $\delta^{56}\text{PFe}$
428 values close to -0.5 ‰, likely reflecting a hydrothermal contribution, as previously suggested
429 by Labatut et al. (2014) for station 24. Northeastern PNG is an active margin with hydrothermal
430 activity (Auzende et al., 2000) with shallow sources able to supply EUC via the NICU (Mackey
431 et al., 2002).

432 The isotopic difference between dissolved and particulate Fe, $\Delta^{56}\text{Fe}_{\text{DFe-PFe}}$, is shown in
433 Figure 7. Except for one data point at the surface this difference is consistently positive, i.e.,

434 DFe is systematically heavier than PFe. This is true for 26 out of 27 data points, including the
435 two data points discussed above with significantly different $\delta^{56}\text{PFe}$ values (attributed to
436 hydrothermal influence). On average this difference is $\Delta^{56}\text{Fe}_{\text{DFe-PFe}} = +0.27 \pm 0.32 \text{ ‰}$ (2SD,
437 $n=27$). This systematic difference suggests a mechanistic link between particulate and dissolved
438 Fe pools, associated with an isotopic fractionation. A kinetic isotopic fractionation associated
439 with an unidirectional reaction would lead to a reaction product isotopically lighter than the
440 reactant. In such a hypothesis, PFe being lighter than DFe, this would imply that PFe is
441 produced from DFe (for instance by precipitation). This is totally unlikely given the
442 predominance of lithogenic PFe sources in this area. We therefore exclude the hypothesis of a
443 kinetic fractionation and conclude that there is an equilibrium isotopic fractionation between
444 PFe and DFe. Equilibrium fractionation implies co-occurrence of chemical fluxes from both
445 phases toward the other. In addition, because DFe is heavier than PFe, the processes responsible
446 for the flux from the particulate to the dissolved phase cannot be associated with an Fe reduction
447 process (that would produce lighter DFe, (Criss, 1999)). This is consistent with the oxygenated
448 water column in this region (Table 2). The PFe to DFe flux is therefore a non-reductive release
449 of dissolved Fe, a process named non-reductive dissolution, NRD, by Radic et al. (2011). The
450 term NRD can refer to dissolution, as well as to other type of processes from the particulate to
451 the dissolved phase, such as desorption. This non-reductive release of dissolved Fe probably
452 reflects processes similar to the reversible scavenging process proposed for Th or rare earth
453 elements (REE) (Bacon and Anderson, 1982; Nozaki et al., 1987; Nozaki and Alibo, 2003).
454 These conclusions have been previously proposed for stations 24, 28 and 30 (Radic et al., 2011;
455 Labatut et al., 2014). The addition of data from five additional western stations reinforces the
456 conclusions drawn from earlier studies and extends the geographic scope of these findings
457 eastward beyond the Bismarck Sea, to as far as 156°E . This confirms the significant role of
458 lithogenic inputs from PNG on the biogeochemistry of the area. These processes govern
459 particulate - dissolved interactions at least up to 1 200 km from the source, within the upper
460 1 000 m of the water column.

461 The non-reductive release of dissolved iron, NRD, at the sediment / water column interface has
462 now been observed in numerous studies as a significant external DFe source. These include the
463 western Pacific (Radic et al., 2011; Labatut et al., 2014; this study), the northwest Atlantic
464 (Conway and John, 2014), the northeast Atlantic (Klar et al., 2018), the southeast Atlantic
465 (Conway et al., 2016), the Southern Ocean (Abadie et al., 2017; Tian et al., 2023) and in the
466 southeast Pacific (John et al., 2018). In the water column, exchange fluxes between particulate
467 and dissolved phases, including non-reductive release of dissolved iron from the particles, have
468 also been proposed in several other studies (Radic et al., 2011; Abadie et al., 2017; Fitzsimmons
469 et al., 2017; John et al., 2018). In all cases, at the sediment/seawater interface and within the
470 water column, the exact processes involved remain unclear. Desorption and ligand-promoted
471 dissolution have been suggested (Abadie et al., 2017; John et al., 2018; Homoky et al., 2021).
472 Additionally, direct comparison of DFe and total PFe isotopic compositions has inherent
473 limitations, as it does not allow us to study the distinct processes related to different PFe phases
474 (lithogenic, biogenic, Fe oxyhydroxides). Those PFe phases are likely not equally involved in
475 particulate - dissolved exchanges. Nevertheless, our analytical approach employs total digestion
476 to guarantee the absence of artifactual isotopic fractionation. The regional geochemical
477 characteristics establish that excess PFe is predominantly lithogenic (Figure 6), with excess
478 DFe correspondingly derived from this source. Although lithogenic iron is conventionally
479 considered refractory, neodymium isotope studies have shown that lithogenic phases do
480 dissolve, even if in small proportions (Lacan and Jeandel, 2005; Rousseau et al., 2015). The
481 excess DFe in the area, from 0.30 to $0.63 \text{ nmol.kg}^{-1}$, affects 19.4 Sv (Germineaud et al., 2016).
482 This leads to a required flux of $\sim 540 \text{ g(DFe).s}^{-1}$. The riverine PFe discharge to this area is about
483 $1.2 \times 10^{11} \text{ g(PFe).day}^{-1}$. Therefore, the dissolution of only 0.04 ‰ of the PFe discharge would
484 be sufficient to account for the observed DFe increase. This very low dissolution rate makes it
485 entirely plausible that the excess DFe originates from the dissolution of lithogenic PFe.



486

487 Figure 7. Differences between the dissolved and particulate of iron isotopic compositions
 488 ($\delta^{56}\text{DFe} - \delta^{56}\text{PFe}$) from the surface to 1 000 m depth in the western equatorial and central
 489 equatorial Pacific.

490

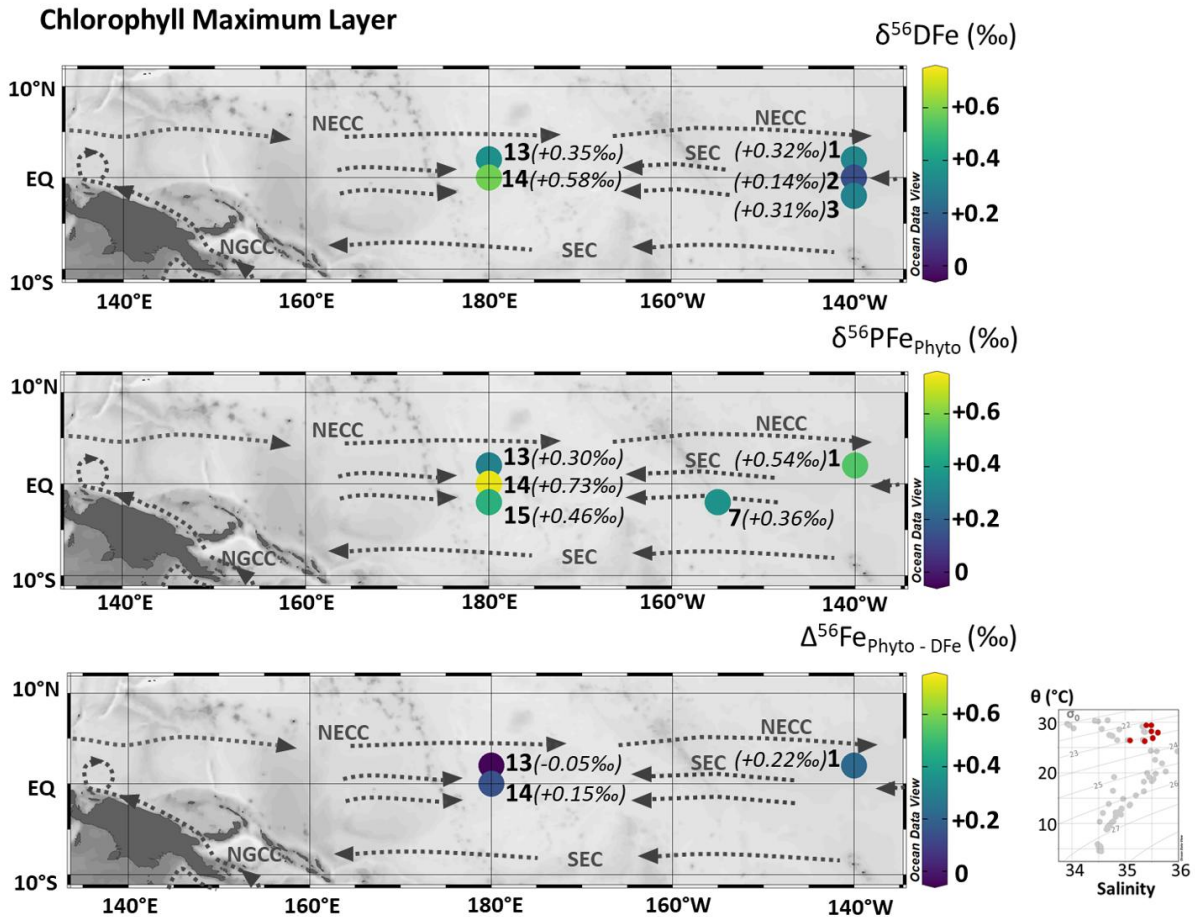
491 5.2. IRON SOURCES AND BIOGEOCHEMICAL DYNAMICS IN THE CENTRAL EQUATORIAL 492 PACIFIC

493 In the central equatorial Pacific, the data are discussed within each of the five density
 494 layers defined in Section 2 in order to take into account different water masses and dominant
 495 currents. Western stations are included in the figures solely to illustrate potential sources to this
 496 central Pacific area. To facilitate interpretation, the $\delta^{56}\text{Fe}$ color scales are different for each
 497 density layer.

498

499 5.2.1. Surface layer, the chlorophyll maximum layer ($< 120 \text{ m}$; $< 23.8 \text{ kg.m}^{-3}$)

500



501

502 Figure 8. From the top to bottom, samples collected in the chlorophyll maximum layer, maps
 503 of $\delta^{56}\text{DFe}$ (‰), $\delta^{56}\text{PFe}_{\text{Phyto}}$ (‰), and the difference between $\delta^{56}\text{PFe}_{\text{Phyto}}$ and $\delta^{56}\text{DFe}$. Station
 504 numbers are displayed next to the colored dots on the map. Main currents are represented: South
 505 Equatorial Current (SEC), North Equatorial CounterCurrent (NECC) and New Guinea Coastal
 506 Current (NGCC). In the bottom right corner, potential temperature (θ , °C) and salinity (S) of
 507 EUCFe samples. Samples in this chlorophyll maximum layer are shown in red. Values are
 508 shown in parentheses due to the large range, which limits color scale readability. Their
 509 measurement uncertainties can be found in Section 5.2.1 and Table 2.

510 Having both dissolved and particulate iron data in the open ocean surface layer,
 511 far from continental inputs, provides an opportunity to quantify isotopic fractionation
 512 associated with biological uptake, i.e., consumption of dissolved Fe by phytoplankton and its
 513 consequent transfer to the particulate pool. We focus on the chlorophyll maximum layer (found
 514 between 10 and 100 m, based on fluorescence data shown in Figure A2), also called the deep
 515 chlorophyll maximum (DCM), where the phytoplanktonic contribution to sampled particles is
 516 likely to be large. During the EUCFe cruise, the phytoplankton community was studied at
 517 station 2 at a depth of 10 meters (Marchetti et al., 2010), and in the chlorophyll maximum layer
 518 at station 2, station 25, and at two other stations lacking iron isotope measurements (0° , 165°E
 519 and 0° , 170°W) (Johnson et al., 2010). The cyanobacteria *Prochlorococcus* and *Synechococcus*
 520 dominate this community, followed by small pennate diatoms such as *C. closterium* and *N.*
 521 *bicapitata* (Johnson et al., 2010; Marchetti et al., 2010). This observation is consistent with
 522 previous studies in this equatorial upwelling region, which report a predominantly
 523 cyanobacteria-based community (Chavez et al., 1990; Landry et al., 1996). Unicellular
 524 diazotrophic cyanobacteria were also identified throughout the cruise, primarily
 525 picocyanobacteria, while the larger *Trichodesmium* was found only in coastal waters (Bonnet
 526 et al., 2009).

527 PFe can be composed of lithogenic, biogenic, and chemogenic fractions. Chemogenic
 528 particles are formed by chemical reactions such as Fe oxyhydroxide precipitations and are
 529 frequently referred to as 'authigenic'. However, this term lacks precision as it merely designates
 530 material formed in situ, which could theoretically include biogenic fractions. Assuming
 531 Aluminum (Al) is entirely lithogenic (Murray et al., 1993; Frank et al., 1995; McManus et al.,
 532 1999; Cardinal et al., 2001; Dammshäuser, 2012), the lithogenic fraction of the particulate iron,
 533 $[PFe]_{\text{lithogenic}}$, is estimated by:

$$534 \quad [PFe]_{\text{lithogenic}} = [PAI]_{\text{measured}} \times \left(\frac{[PFe]}{[PAI]} \right)_{\text{reference material}} \quad (\text{Equation 3})$$

535 where $[PAI]_{\text{measured}}$ is the measured particulate Al concentration and $[PFe]/[PAI]_{\text{reference material}}$ is
 536 the ratio in a reference lithogenic material. Surface currents in our studied area are mainly
 537 eastward in the western Pacific and westward in the central Pacific. We therefore looked for
 538 reference lithogenic material on both the western and eastern boundaries of the Pacific basin.
 539 The Fe/Al ratios of igneous rocks from Papua New Guinea (Tiangang et al., 2024) and of
 540 igneous rocks from the Galapagos Islands and the southwestern Andes basins of Peru (Wilson
 541 et al., 2022; Ccancapa-Cartagena et al., 2023) are equal to 0.502 mol.mol⁻¹ and 0.499 mol.mol⁻¹
 542 respectively. Given the similarity of these ratios, we utilized an average value of 0.50 mol.mol⁻¹
 543 for all samples.

544 In the chlorophyll maximum layer, we found an average of 42 % mol.mol⁻¹ of particulate iron
 545 (PFe) is lithogenic (Table A3). The remaining 58 % mol.mol⁻¹ can be attributed to biogenic and
 546 chemogenic sources. The chemogenic fraction cannot be distinguished and quantified in the
 547 present study (this would have required, for example, direct measurements of phytoplankton
 548 stoichiometry and phosphorus), and there is no known isotopic signature specific to this
 549 chemogenic fraction in the literature (which is essential for Equation 4)., Because we are
 550 looking at samples taken in the chlorophyll maximum, we will assume in the following that the
 551 chemogenic Fe is negligible. This assumption is supported by observations reporting minimum
 552 chemogenic contribution in the chlorophyll maximum layer (Sofen et al., 2013) and modelling
 553 work estimating that the biogenic fraction dominates in the central equatorial Pacific (Tagliabue
 554 et al, 2023). We also assume that biogenic Fe is entirely phytoplanktonic Fe (PFe_{Phyto}) and
 555 assuming mass conservation, $\delta^{56}PFe_{\text{Phyto}}$ can be estimated from:

$$556 \quad [PFe]_{\text{Phyto}} \cdot \delta^{56}PFe_{\text{Phyto}} \approx [PFe] \cdot \delta^{56}PFe - [PFe]_{\text{lithogenic}} \cdot \delta^{56}PFe_{\text{lithogenic}} \quad (\text{Equation 4})$$

557 where $[PFe]$ and $\delta^{56}PFe$ are the measured particulate Fe concentration and isotopic composition.
 558 The lithogenic PFe is assumed to be characterized by average crustal signature $\delta^{56}PFe_{\text{lithogenic}} =$
 559 $+0.07 \pm 0.02 \text{ ‰}$ (Poitrasson, 2006). The estimated isotope compositions of phytoplanktonic
 560 PFe are shown in Figure 8 and Table A3. $\delta^{56}PFe_{\text{Phyto}}$ varies from $+0.30 \pm 0.12 \text{ ‰}$ to
 561 $+0.73 \pm 0.17 \text{ ‰}$. Propagation of uncertainties for Fe and Al concentrations and Fe isotopes in
 562 both the samples and the reference material implies uncertainties for $\delta^{56}PFe_{\text{Phyto}}$ significantly
 563 higher than those of our initial data.

564 At three stations, the isotope data are available for both the dissolved and the
 565 phytoplanktonic iron. This allows an estimate of isotope fractionation associated with
 566 phytoplankton uptake. Assuming two simple isotopic models, either an equilibrium
 567 fractionation model (implying bidirectional chemical reactions) or a kinetic fractionation model
 568 in which phytoplankton is the instantaneous product of DFe (implying unidirectional chemical
 569 reactions), the isotopic fractionation can be calculated, with the same simple equation (Hayes,
 570 2004):

$$571 \quad \Delta^{56}Fe_{\text{Phyto-DFe}} = \delta^{56} PFe_{\text{Phyto}} - \delta^{56}DFe \quad (\text{Equation 5})$$

572 This leads to $\Delta^{56}\text{Fe}_{\text{Phyto-DFe}} = +0.22 \pm 0.21 \text{ ‰}$ at station 1, $-0.05 \pm 0.14 \text{ ‰}$ at station 13 and
573 $+0.15 \pm 0.19 \text{ ‰}$ at station 14, with a grand average value of $\Delta^{56}\text{Fe}_{\text{Phyto-DFe}} = +0.11 \pm 0.28 \text{ ‰}$
574 (2SD, n=3) (Figures 8 and Table A3). Given the uncertainties, we cannot conclude that there is
575 isotopic fractionation associated with biological uptake, but our data indicate that if it exists, it
576 is small and lies between -0.17 and $+0.39 \text{ ‰}$ ($+0.11 \pm 0.28$) at a 95% confidence level.

577 These results can be compared with previous studies. Some suggest preferential uptake
578 of light and others of heavy isotopes. From the same cruise, Radic et al. (2011) found
579 $\Delta^{56}\text{Fe}_{\text{Phyto-DFe}} = -0.25 \pm 0.10 \text{ ‰}$ (2SD) with one model and $-0.13 \pm 0.11 \text{ ‰}$ (2SD) with a second
580 model. While the first model was based solely on DFe data, the second incorporated PFe data
581 assuming PFe was exclusively phytoplanktonic, whereas our results indicate a substantial
582 lithogenic contribution at the open ocean stations (Table A3). [Additional data and novel
583 methodological approaches have refined these estimates.](#) Off New Zealand, during the annual
584 spring bloom, Ellwood et al. (2015) estimated an isotopic fractionation of -0.54 ‰ . In [that study](#)
585 the isotopic signatures of the particles were used, but not corrected for their lithogenic fractions,
586 despite proximity to the mainland, and fractionation uncertainties were not discussed. In two
587 Antarctic coastal polynyas, preferential uptake of light isotopes [was](#) suggested based on water
588 mass DFe signatures alone (without PFe data), with isotopic fractionation of -1 ‰
589 ($\alpha = \delta^{56}\text{Fe}_{\text{Biomass}} / \delta^{56}\text{Fe}_{\text{Seawater}} = 0.999$) (Sieber et al., 2021) and of -1.8 to -1 ‰ ($\alpha = 0.9982$ to
590 0.9990) (Tian et al., 2023). However, both studies highlighted the co-occurrence of multiple
591 mechanisms and, therefore, of several isotopic fractionation processes in the surface layer.
592 Ellwood et al. (2020) conducted a study using both DFe and PFe isotope data in a 1-D model,
593 and found isotopic fractionation values for biological uptake ranging from -1 ‰ (in a simplified
594 model considering only biological uptake) to -0.6 ‰ when using a more sophisticated model
595 representing additional processes (regeneration, scavenging and complexation) in a cold-core
596 eddy in the Southern Ocean. Again, fractionation uncertainties were not discussed in these three
597 studies. Finally, in the North Atlantic, two studies suggested a positive fractionation
598 (contrasting with the previous studies) based on water mass DFe signatures (no PFe data) and
599 without quantification (Conway and John, 2014; Klar et al., 2018). [Culture experiments
600 examining isotopic fractionation by several diatom and a coccolithophore species \(not the
601 dominant species in our samples \(Johnson et al., 2010; Marchetti et al., 2010\)\) revealed ‘no
602 clear relationship to species, growth rate, or Fe concentration’ for biological uptake, possibly
603 due to the sensitivity of kinetic isotope effects \(John et al., 2024\). During these experiments,
604 biological uptake induced smaller fractionation \(\$-1.3 \text{ ‰}\$ to \$+0.60 \text{ ‰}\$, mean \$+0.20 \pm\$
605 \$0.38 \text{ ‰}\$, 1SD, n=62\) compared to abiotic processes \(approximately \$-4 \text{ ‰}\$ to \$+5 \text{ ‰}\$ \). These
606 laboratory observations align with our in situ observations, although a comparison is not
607 straightforward because iron acquisition processes are very different in cyanobacteria \(Sutak et
608 al., 2020\). These authors suggested that seawater \$\delta^{56}\text{Fe}\$ may not be greatly impacted by
609 biological uptake \(John et al., 2024\); a conclusion consistent with the findings of Lacan et al.,
610 2008 and Radic et al., 2011.](#)

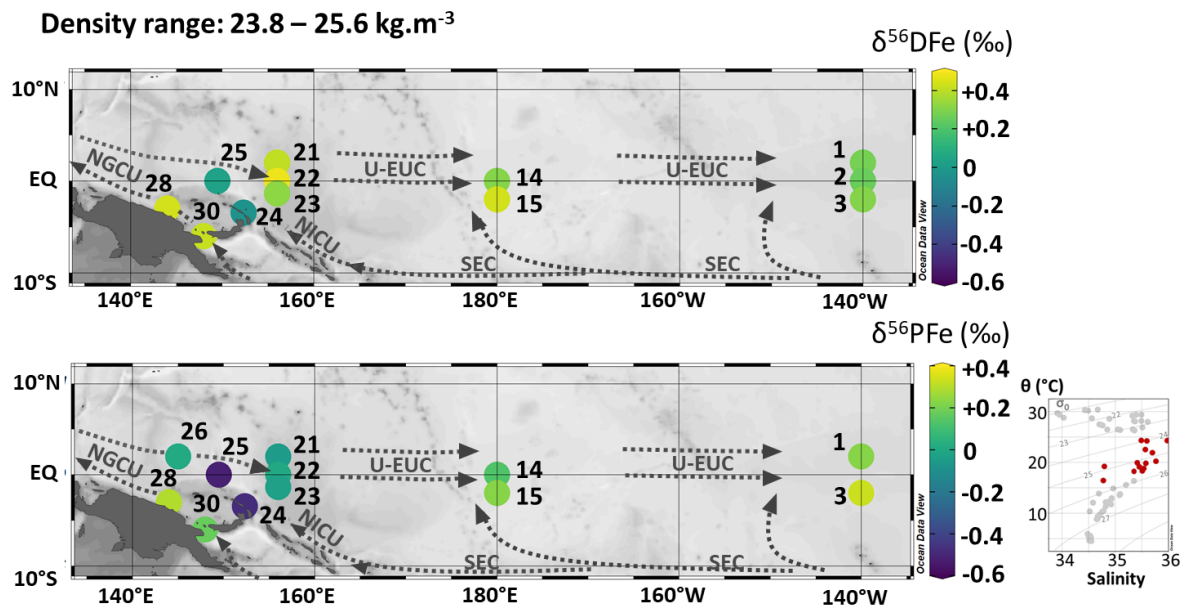
611 The differences in biological fractionation probably reflect variations in phytoplankton
612 community composition, ligand types (John et al., 2024), regional variability, and
613 methodological approaches such as the direct measurement of particles and the consideration
614 of their phases. Potential iron fractionation during biological uptake, if it occurs, may depend
615 on numerous parameters, including species-specific iron acquisition processes (Sutak et al.,
616 2020), as well as pH, ligand, and reductant types, which strongly influence kinetic isotope
617 effects (John et al., 2024). Our study region is particularly challenging in this regard, as it is a
618 cyanobacteria-dominated system where isotopic fractionation processes remain poorly
619 understood (Mulholland et al., 2015; Swanner et al., 2017). Iron isotope fractionation by
620 diazotrophic cyanobacteria has not been investigated, despite these organisms contributing
621 disproportionately to Fe uptake relative to their numerical abundance (Lory et al., 2022). The
622 present analysis does not allow us to draw conclusions regarding a preferential uptake of heavy

623 or light iron isotopes during biological uptake. However, our results confirm that this
 624 fractionation is small, likely not larger than a few tenths of a per mil. They align with a [previous](#)
 625 study, in the Southern Ocean, where fractionation [had](#) a small amplitude,
 626 $|\Delta^{56}\text{Fe}_{\text{Phyto-DFe}}| < 0.32 \text{ ‰}$, with no conclusion about the direction (Lacan et al., 2008), [and culture](#)
 627 [experiments](#) (John et al., 2024). Our analysis emphasizes the importance of taking into account
 628 error propagations and lithogenic contributions to the particulate phases, in the chlorophyll
 629 maximum in the open ocean.

630

631 5.2.2. Subsurface layer (110 – 220 m; 23.8 – 25.6 kg.m⁻³), upper EUC

632



633

634 Figure 9. Map of dissolved ($\delta^{56}\text{DFe}$) and particulate ($\delta^{56}\text{PFe}$) iron isotopes for samples with
 635 potential densities between 23.8 and 25.6 kg.m⁻³. Station numbers are displayed next to the
 636 colored dots. Main currents are represented: the upper Equatorial Undercurrent (U-EUC), the
 637 South Equatorial Current (SEC), the New Guinea Coastal Undercurrent (NGCU) and the New
 638 Ireland Coastal Undercurrent (NICU). In the bottom right corner, potential temperature (θ , °C)
 639 and salinity (S) of EUCFe samples. Samples in this density layer are shown in red.

640 The subsurface layer is composed of three water masses: the South Pacific Tropical
 641 Water (SPTW) (stations 3 and 15), the South Pacific Equatorial Water (SPEW) (stations 2, 14,
 642 21, 22, 23, 24, 25, 28 and 30) and the North Pacific Equatorial Water (NPEW) (stations 1 and
 643 26) (Figure 9). At the equator, seawater within SPEW is subject to substantial renewal as it
 644 flows eastward from the western Pacific (140°E) to the central equatorial Pacific (140°W)
 645 (Tsuchiya et al., 1989; Grenier et al., 2011). This renewal is largely driven by equatorial
 646 upwelling which creates divergence in subsurface waters and subsequently generates
 647 meridional currents from both the northern and southern subtropical gyres toward the equator.
 648 These gyres ventilate the upper Equatorial Undercurrent (U-EUC), contributing approximately
 649 9 Sv of the total 28 Sv contribution at 140°W, accounting for nearly one third of the upper EUC
 650 flow (Grenier et al., 2011).

651 We observed that $\delta^{56}\text{DFe}$ values were equal within uncertainties along the meridional
 652 transects between 2°N and 2°S (+0.40 ‰, +0.37 ‰ and +0.28 ‰ at 156°E, 180°E and 140°W,
 653 respectively) and similar consistency is observed for $\delta^{56}\text{PFe}$ (-0.03 ‰, +0.18 ‰ and +0.28 ‰

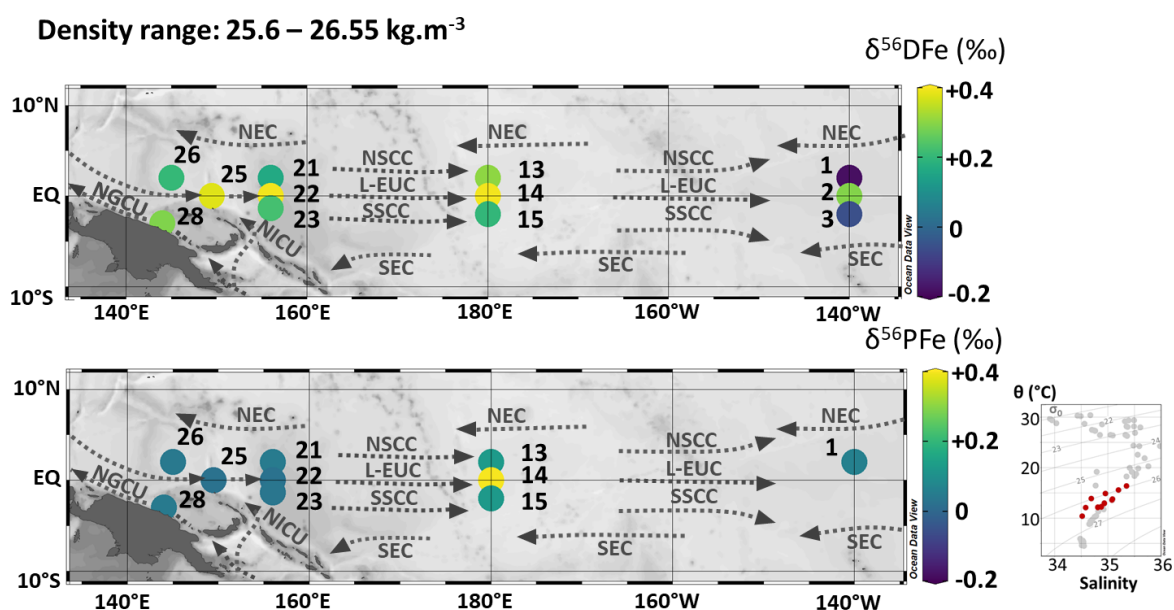
654 at the three same sections, Figure 9 and Table 2). This isotopic homogeneity is consistent with
 655 the prevailing ocean circulation in the subsurface layer. Zonally, a slight decrease of $\delta^{56}\text{DFe}$
 656 values and a slight increase of $\delta^{56}\text{PFe}$ values were observed eastward.

657 A comparison of DFe isotopic compositions ($\delta^{56}\text{DFe}$) in EUCFe samples with data from
 658 the subtropical gyres provides further insight. While no data are available for the north
 659 subtropical gyre, this density layer has been documented in the south subtropical gyre along
 660 170°W (GP19 cruise) at 10°S (Station 19) with $\delta^{56}\text{DFe} = +0.64 \pm 0.32 \text{ ‰}$, and at the equator
 661 (Station 21) with $\delta^{56}\text{DFe} = +0.70 \pm 0.35 \text{ ‰}$ (GEOTRACES Intermediate Data Product Group,
 662 2023). These two datapoints are in good agreement. They may appear to be significantly
 663 different from our data ($\sim 0.37 \pm 0.1 \text{ ‰}$ at 180°E), however given their uncertainties, they are
 664 in reasonable agreement. They do not help explain the slight eastward decrease of $\delta^{56}\text{DFe}$ along
 665 the equator described above.

666 Overall, despite small variations, these observations suggest a relatively wide isotopic
 667 homogeneity at subsurface depths (110 – 220 m) likely driven by equatorial upwelling and the
 668 subsequent meridional transport of seawater.

669

670 5.2.3. Lower part of EUC: Central Waters (170 – 320 m; 25.6 – 26.55 kg.m⁻³)



671

672 Figure 10. Map of dissolved ($\delta^{56}\text{DFe}$) and particulate ($\delta^{56}\text{PFe}$) iron isotopes for samples
 673 with potential densities between 25.6 and 26.55 kg.m⁻³. Station numbers are displayed next to
 674 the colored dots. Main currents are represented: the lower Equatorial Undercurrent (L-EUC),
 675 the North and South Subsurface Countercurrents (NSCC and SSCC), the North and South
 676 Equatorial Current (NEC and SEC), the New Guinea Coastal Undercurrent (NGCU) and the
 677 New Ireland Coastal Undercurrent (NICU). In the bottom right corner, potential temperature
 678 (θ , °C) and salinity (S) of EUCFe samples. Samples in this density layer are shown in red.

679

680 The density layer between 25.6 and 26.55 kg.m⁻³ is composed of two water masses: the
 681 Western South Pacific Central Water (WSPCW) (stations 1, 2, 3, 14, 15, 22, 23, 25, 28) and the
 682 North Pacific Central Water (NPCW) (stations 13, 21, 26) (Figure 2). WSPCW is characterized
 683 by a salinity maximum of central waters while NPCW represents a salinity minimum. The lower

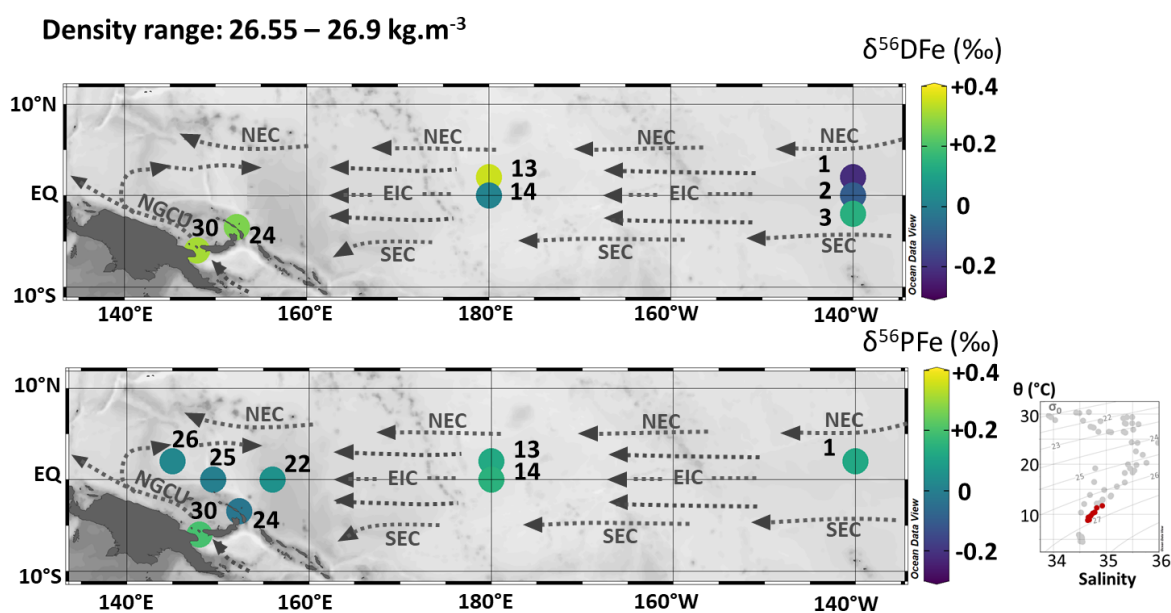
684 part of the EUC (L-EUC) is located in this density layer (Figure 10). This current is of particular
685 importance, since it is the major vector for Fe transport along the equator from the western to
686 the eastern Pacific. The lower EUC is not significantly influenced by the equatorial upwelling
687 in the western equatorial Pacific, and water mostly originates from the PNG region (Grenier et
688 al., 2011).

689 Along the equator, at stations 25, 22, 14 and 2, samples have similar DFe isotopic
690 composition (around +0.36 ‰), highlighting the lack of significant additional Fe sources to the
691 lower EUC (Tsuchiya et al., 1989; Radic et al., 2011). $\delta^{56}\text{DFe}$ values are equal within
692 uncertainties (Figure 10 and Table 2). This suggests that the $\delta^{56}\text{DFe}$ signature is maintained
693 over long distances within the EUC, a pattern previously reported by Radic et al. (2011) at two
694 stations, and here confirmed as far east as 140°W. In contrast, $\delta^{56}\text{PFe}$ cannot be evaluated at
695 station 2 due to missing PFe data, and values from stations 22 and 14 displayed significantly
696 different values. These findings confirm the central role of the EUC for DFe transport across
697 the Pacific. While earlier studies based on Fe concentrations suggested such transport (Slemons
698 et al., 2012), isotopic data now confirm this conclusion and the fact that dissolved iron isotopic
699 signature may be preserved, in over more than 7 800 km (from station 25 to station 2). Long
700 distance preservation of $\delta^{56}\text{DFe}$ signature has been underlined before for deeper layers, notably
701 in the North Pacific and eastern Pacific with Fe transport from sedimentary and hydrothermal
702 sources (Fitzsimmons et al., 2017; John et al., 2018; Sieber et al., 2024). Such a long distance
703 of preservation of the $\delta^{56}\text{DFe}$ signature had never been observed before.

704 Samples from stations 1 and 3 differ significantly from the other samples. They are
705 characterized by negative dissolved iron isotopic compositions (-0.19 and -0.06 ‰) (Figure 10
706 and Table 2). They are characterized by oxygen concentrations which are notably lower than
707 those typically found in the core of the EUC (43 and 25 $\mu\text{mol.kg}^{-1}$, compared to typical values
708 around 130 $\mu\text{mol.kg}^{-1}$). The currents supplying these stations, the SEC and NEC, originate
709 from the east. These three observations support the conclusion that their Fe content may
710 originate, at least partially, from the Californian and/or Peruvian oxygen minimum zones
711 (OMZ). Those have been documented before, with negative or zero $\delta^{56}\text{DFe}$ values in the
712 Californian OMZ (John et al., 2012), and DFe concentrations and isotopic compositions, around
713 1 nM and -0.5 ‰, observed around 12°S near the Peruvian coast (85 to 80°W) during the GP16
714 cruise (John et al., 2018). As above, this suggests a $\delta^{56}\text{DFe}$ signature preservation over long
715 distances, on the order of 6,400 km.

716 In the density layer of the lower EUC, iron isotopes reveal the presence of two distinct
717 Fe sources in the central Pacific, lithogenic inputs from Papua New Guinea transported within
718 the EUC, and also a likely additional eastern source from the eastern Pacific oxygen minimum
719 zones.

720 **5.2.4. South Antarctic Mode Water and Lower Central Waters (340 – 480 m; 26.55 –**
 721 **26.9 kg.m⁻³)**



722
 723 Figure 11. Map of dissolved ($\delta^{56}\text{DFe}$) and particulate ($\delta^{56}\text{PFe}$) iron isotopes for samples with
 724 potential densities between 26.55 and 26.9 kg.m⁻³. Station numbers are displayed next to the
 725 colored dots. Main currents are represented: the Equatorial Intermediate Current (EIC), the
 726 North and South Equatorial Current (NEC and SEC), and the New Guinea Coastal Undercurrent
 727 (NGCU). In the bottom right corner, potential temperature (θ , °C) and salinity (S) of EUCFe
 728 samples. Samples in this density layer are shown in red.

729 The density layer between 26.55 and 26.9 kg.m⁻³ is composed of two water masses: the
 730 South Antarctic Mode Water (SAMW) (stations 22, 24, 25) and the Western South Pacific
 731 Central Water (WSPCW) (stations 1, 2, 3, 13, 14, 26, 30). In contrast to the shallower density
 732 layers, where currents predominantly flow eastward, this deeper layer exhibits westward
 733 currents (Figure 11).

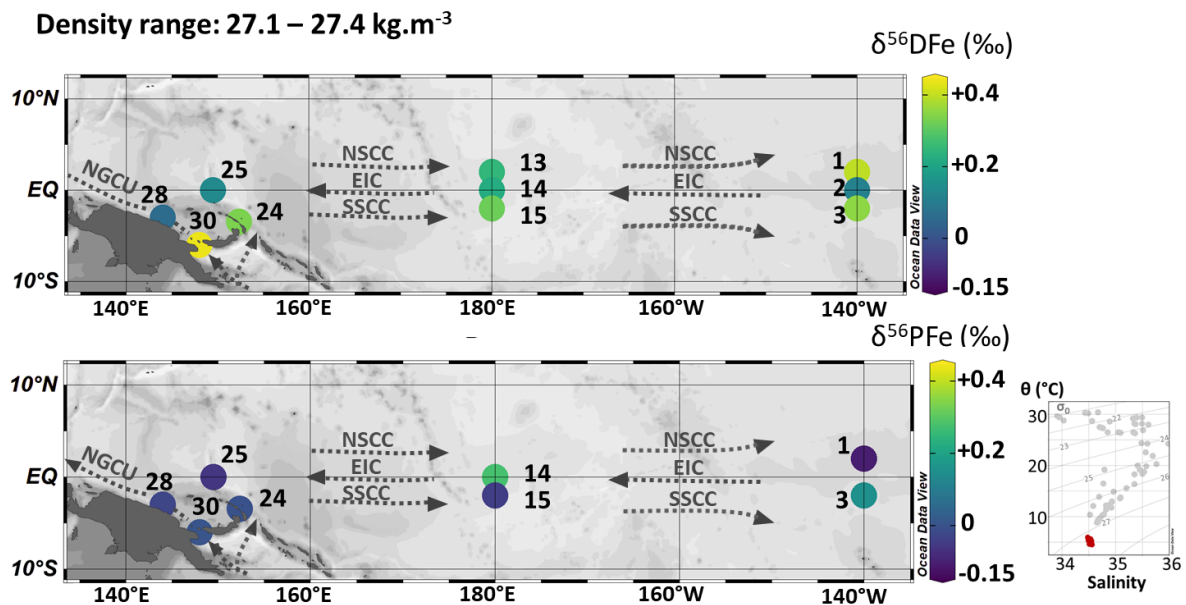
734 DFe isotopic compositions at stations 1, 2, 3, 13 and 14 were variable: negative or near
 735 zero $\delta^{56}\text{DFe}$ at stations 1, 2 and 14 (between -0.22 and +0.01 ‰) and positive $\delta^{56}\text{DFe}$ at stations
 736 3 and 13 (+0.14 and +0.35 ‰) (Figure 11 and Table 2). $\delta^{56}\text{DFe}$ values increased westward from
 737 station 1 (-0.22 ± 0.09 ‰) to station 13 (+0.35 ± 0.07 ‰) and from station 2 (-0.10 ± 0.07 ‰)
 738 to station 14 (+0.01 ± 0.07 ‰). This westward increase in $\delta^{56}\text{DFe}$ follows the predominant
 739 direction of zonal currents. It is consistent with data from GP19 at 170°W at the equatorial
 740 station 21 (-0.07 ± 0.05 ‰, depth of 469 m) (GEOTRACES Intermediate Data Product Group,
 741 2023). In contrast, $\delta^{56}\text{PFe}$ values at stations 1, 13, and 14 were indistinguishable from one
 742 another and similar to the UCC reference value. Samples from stations 1, 2, 3, 13 and 14
 743 exhibited low oxygen concentrations (< 64 $\mu\text{mol.kg}^{-1}$). In contrast, samples from the western
 744 equatorial Pacific (stations 22, 24, 25, 26 and 30) had oxygen concentrations ranging from 101
 745 to 162 $\mu\text{mol.kg}^{-1}$.

746 These isotopic and oxygen observations suggest an Fe source from the eastern Pacific
 747 oxygen minimum zones (OMZ) and a progressive decline in the influence of eastern Pacific
 748 waters with the increase of $\delta^{56}\text{DFe}$ westward. It is consistent with our understanding of large-
 749 scale circulation patterns at these depths across the Pacific basin, and with the signatures of
 750 these areas as described above (John et al., 2012, 2018). In contrast, particulate data were

751 indistinguishable from those of the UCC all along the EUCCFe cruise and therefore do not reflect
752 hydrodynamic structures.

753

754 **5.2.5. Intermediate Waters (SeqIW and AAIW) (720 – 1 000 m; 27.1 – 27.4 kg.m⁻³)**



755

756 Figure 12. Map of dissolved ($\delta^{56}\text{DFe}$) and particulate ($\delta^{56}\text{PFe}$) iron isotopes for samples with
757 potential densities between 27.1 and 27.4 kg.m⁻³. Station numbers are displayed next to the
758 colored dots. Main currents are represented: the Equatorial Intermediate Current (EIC), the
759 North and South Subsurface Countercurrents (NSCC and SSCC), and the New Guinea Coastal
760 Undercurrent (NGCU). In the bottom right corner, potential temperature (θ , °C) and salinity (S)
761 of EUCFe samples. Samples in this density layer are shown in red.

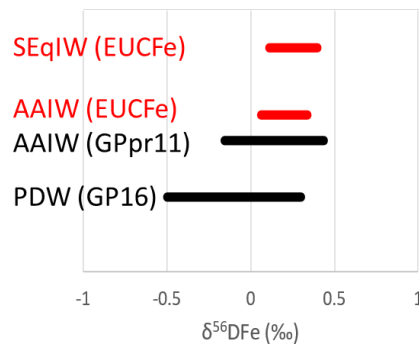
762 The density layer between 27.1 and 27.4 kg.m⁻³ is composed of two intermediate water
763 masses: the South Equatorial Intermediate Water (SeqIW) (stations 1, 2, 3, 13, 14, 15, 25) and
764 the Antarctic Intermediate Water (AAIW) (stations 24, 28, 30) (Figure 12). In this layer, the
765 Equatorial Intermediate Current (EIC), a westward current, is surrounded by two eastward
766 currents, the North and South Subsurface Countercurrents (NSCC and SSCC). The water of the
767 EIC is sheared between the NSCC and SSCC currents at about 2°N and 2°S, causing mixing of
768 water brought in by different currents.

769 Along the equator, a uniform $\delta^{56}\text{DFe}$ signature was observed between stations 2, 14 and
770 25, around +0.15 ‰. North and south of it, in the NSCC and the SSCC, the $\delta^{56}\text{DFe}$ signatures
771 were significantly heavier, around +0.32 ‰ and +0.34 ‰ respectively, and did not vary
772 significantly zonally. This is consistent with the hydrodynamic structure (westward flowing
773 EIC at the Equator and eastward flowing NSCC and SSCC at 2°N and 2°S) and may also reflect
774 slightly lighter signatures originating from the eastern Pacific compared to the western Pacific.
775 In contrast, no such consistency was observed for the $\delta^{56}\text{PFe}$ values.

776 $\delta^{56}\text{DFe}$ of the AAIW and SeqIW from this study are compared with data from the South
777 Pacific, GPpr11 (in the Southern Ocean, south of Australia) and GP16 cruises (John et al., 2018;
778 Ellwood et al., 2020) in Figure 13. The EUCFe AAIW signature (sampled at the western
779 stations 24, 28 and 30 only) fell within the range of data previously reported, but with less
780 variability (from +0.06 to +0.44 ‰, with an average of +0.28 ‰). As explained previously this
781 likely reflects the impact of particulate - dissolved reversible exchange and non-reductive

782 dissolution processes which buffer the isotopic signature of this water mass toward about
783 +0.3 ‰, in the PNG area.

784 The SEqIW (sampled at stations 1, 2, 3, 13, 14, 15, and 25) results from the mixing
785 between the AAIW and the Pacific Deep Water (PDW). Its signatures fall within the range
786 observed for those waters masses in previous studies, but they fall in the heavy [range](#) of those
787 [values](#) and again have a smaller variability (from +0.11 to +0.40‰, average value of +0.24‰).
788 This confirms 1) the large contribution of AAIW to the iron content of SEqIW and the fact that
789 AAIW transits from the South through the PNG area and notably Vitiaz Strait before spreading
790 in the equatorial band (Tomczak and Godfrey, 2003; Bostock et al., 2010), and 2) that the PDW
791 contributing to the SEqIW reaches the Equatorial band with minor contribution from eastern
792 Pacific OMZ derived iron, characterized by light isotopic signatures (John et al 2018).



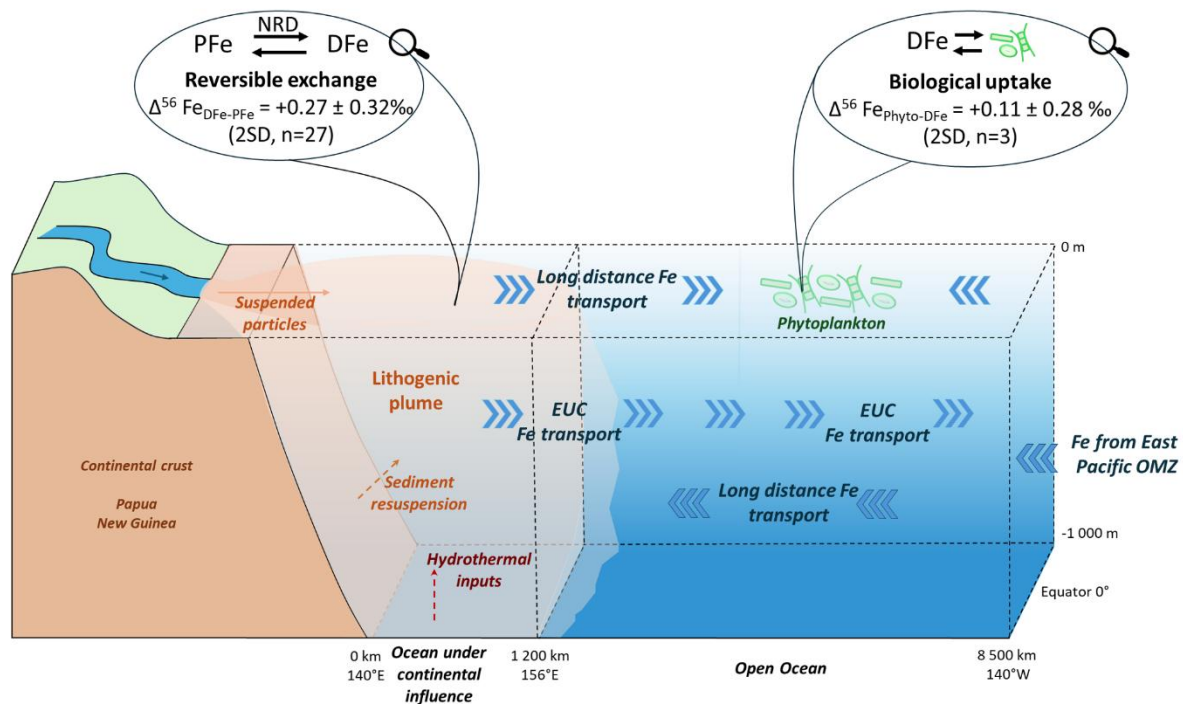
793

794 Figure 13. Comparison of $\delta^{56}\text{DFe}$ values in different water masses: the SEqIW sampled during
795 EUCFe cruise (this study), the AAIW sampled during EUCFe (this study) and GPpr11 cruises
796 (Ellwood et al., 2020) and the PDW sampled during GP16 cruise (John et al., 2018).

797

798 6. CONCLUSIONS

799 The main conclusions resulting from [this](#) study of concentrations and isotope
800 compositions for iron in the upper 1 000 meters of the water column between 140°E and 140°W
801 [are shown in Figure 14.](#)



802

803 Figure 14. Illustration of Fe transport and transformation along the EUCFe cruise along the equator from the surface to 1 000 meters depth. OMZ stands for oxygen minimum zone.
804

805 The goal of the EUCFe cruise was to determine the distribution of Fe along the equator
806 between Papua New Guinea (PNG) and 140°W and to investigate the role of the Equatorial
807 Undercurrent (EUC) in the Fe supply to the central equatorial Pacific. This study reports
808 seawater Fe concentrations and isotopic compositions ($\delta^{56}\text{Fe}$) in both the dissolved (DFe) and
809 particulate (PFe) phases. By adding data from 11 additional stations, this work significantly
810 enriches the data previously published from four stations on the same cruise (Radic et al., 2011;
811 Labatut et al., 2014) and introduces a novel suggestion about an iron source from the eastern
812 Pacific OMZ. The isotopic compositions ranged from -0.25 to +0.79 ‰ for dissolved iron and
813 from -0.56 to +0.48 ‰ for particulate iron. Two distinct groups of stations were identified on
814 the basis of Fe concentrations: western Pacific stations displaying PFe and DFe concentrations
815 approximately seven times and twice larger than typical open ocean concentrations,
816 respectively (stations 21, 22, 23, 24, 25, 26, 28, and 30, all located within 1 200 km of the Papua
817 New Guinea coast) and central Pacific open ocean stations, with PFe and DFe typical of the
818 open ocean (stations 1, 2, 3, 7, 13, 14, and 15).

819 In the western equatorial Pacific, a large predominance of PFe concentrations over that
820 of DFe was observed (80 % mol.mol⁻¹ PFe compared to total Fe, on average). The isotope
821 signature of PFe approached that of the UCC confirming the major influence of previously
822 documented lithogenic inputs from PNG in this area (Milliman et al., 1999; Slemons et al.,
823 2012). At two stations, distinctly light $\delta^{56}\text{DFe}$ and $\delta^{56}\text{PFe}$ signatures suggested local
824 hydrothermal inputs. At all stations of this western area, a systematic positive difference
825 between $\delta^{56}\text{DFe}$ and $\delta^{56}\text{PFe}$ was observed, $\Delta^{56}\text{Fe}_{\text{DFe-PFe}} = +0.27 \pm 0.32\text{‰}$ (2SD, n=27). This is
826 interpreted as the result of equilibrium isotopic fractionation, in other words the co-occurrence
827 of chemical fluxes from both phases toward the other. This probably reflects processes similar
828 to the reversible scavenging process proposed for Th or REE (Bacon and Anderson, 1982;
829 Nozaki et al., 1987; Nozaki and Alibo, 2003), as previously proposed (Abadie et al., 2017).
830 Desorption and/or ligand-promoted dissolution are potential mechanisms, though the exact
831 processes involved remain unclear (Abadie et al., 2017; Homoky et al., 2021). Isotopic
832 signatures suggest that Fe is primarily released via non-reductive release of dissolved Fe from

833 suspended particles and/or oxic sediment. New data from 11 additional stations demonstrate
834 that this process extends up to 1 200 km from the Papua New Guinea coast.

835 In the open ocean, between 180°E and 140°W, data from the chlorophyll maximum
836 layer were used to estimate isotopic fractionation associated with phytoplankton uptake. Our
837 data suggest that isotopic fractionation during phytoplankton uptake is small, on the order of a
838 few tenths of per mil. Estimates of fractionation due to biological uptake must include
839 consideration of phytoplankton composition, dominated here by cyanobacteria. Just below this
840 layer, within the upper EUC, $\delta^{56}\text{Fe}$ values remain homogeneous across a broad region spanning
841 2°N to 2°S and 156°E to 140°W, consistent with equatorial upwelling and meridional Fe inputs.
842 In the lower EUC, a DFe isotopic signature of $\sim +0.36\%$, from Papua New Guinea eastward
843 to at least 140°W, confirms the origin of the DFe carried within this current toward the HNLC
844 area. However, an additional Fe source was identified bordering the lower EUC at 2°N and 2°S
845 likely originating from the oxygen minimum zones (OMZ) of the eastern Pacific. This OMZ
846 Fe source appears to be also traced deeper within central waters (200–500 m depth). The
847 preservation of distinct Fe isotopic signatures over unprecedented long distances, 7 800 km, is
848 a key observation of this study. Finally, the limited variability of the $\delta^{56}\text{DFe}$ signatures in
849 intermediate waters, averaging $+0.24\%$, confirms the major influence of AAIW transiting
850 through the PNG area in the intermediate waters in the EUCFe area.

851 In conclusion, this study demonstrates the substantial influence of lithogenic inputs
852 along ocean margins, where the water column (at least down to 1000 m) is affected by
853 equilibrium fractionation between dissolved and particulate phases. It suggests the significance
854 of non-reductive processes releasing dissolved iron from particulate iron. This non-reductive
855 dissolution (NRD), occurs either at the sediment/seawater interface (i.e., external sources), or
856 within the water column (i.e., internal processes). This highlights the need for a better
857 understanding of these non-reductive DFe – PFe interactions, through in situ explorations,
858 experimental work and biogeochemical modelling. Such processes likely influence the
859 biogeochemical cycling of multiple elements. This study allowed identification of long-distance
860 iron transport by ocean currents from an ocean margin and clarified the key role of the
861 Equatorial Undercurrent (EUC). Finally, it suggested minor fractionation associated to
862 phytoplankton uptake.

863

865 **Table A1.** Sensitivity tests for different scenarios. Mean PFe concentration, Flux PFe_{SWout}, the
 866 required external sources flux, Flux PFe_{aerosol} and Flux PFe_{riverine} contribution to required
 867 external sources (% g.g⁻¹) according to different calculation methods. Go-Flo replicates are
 868 duplicate samples taken at sea, from the same cast.

	Go-Flo bottle replicates considered separately and with the highest value (29.45 nmol.kg ⁻¹)	Go-Flo bottle replicates considered separately and without the highest value (29.45 nmol.kg ⁻¹)	Go-Flo bottle replicates averaged and with the highest value (29.45 nmol.kg ⁻¹)	Go-Flo bottle replicates averaged and without the highest value (29.45 nmol.kg ⁻¹)
Mean PFe concentration (nmol.kg ⁻¹)	3.6 ± 4.8 (1SD)	2.9 ± 2.3 (1SD)	3.8 ± 5.0 (1SD)	3.0 ± 2.5 (1SD)
Flux PFe _{SWout} (10 ⁶ g.day ⁻¹)	337.9	272.2	356.7	281.6
Required external sources flux:				
Flux PFe _{SWout} - Flux PFe _{SWin} (10 ⁶ g.day ⁻¹)	323.5	257.8	342.2	267.1
Aerosol PFe flux contribution to required external sources (% g.g ⁻¹)	82.9	104.0	78.3	100.3
Riverine PFe flux contribution to required external sources (% g.g ⁻¹)	37,099.0	46,556.2	35,064.0	44,920.3

869

870 **Table A2.** Daily precipitation rates (mm.day⁻¹) over the entire region considered in the box
 871 model (133°E–177°W, 9°S–15°N) from September 20 to 30, 2006. The data was obtained from
 872 Nasa Giovanni data product TRMM (3B42 Daily v7)
 873 (<https://giovanni.gsfc.nasa.gov/giovanni/>).

Date	Precipitation Rate (TRMM 3B42 Daily v7) access in December 2025 from Nasa Giovanni data product TRMM (mm.day ⁻¹)
September 20, 2006	7.5
September 21, 2006	7.7
September 22, 2006	10.6
September 23, 2006	8.3
September 24, 2006	10.2
September 25, 2006	9.0
September 26, 2006	11.4
September 27, 2006	13.9

September 28, 2006

14.4

September 29, 2006

16.5

September 30, 2006

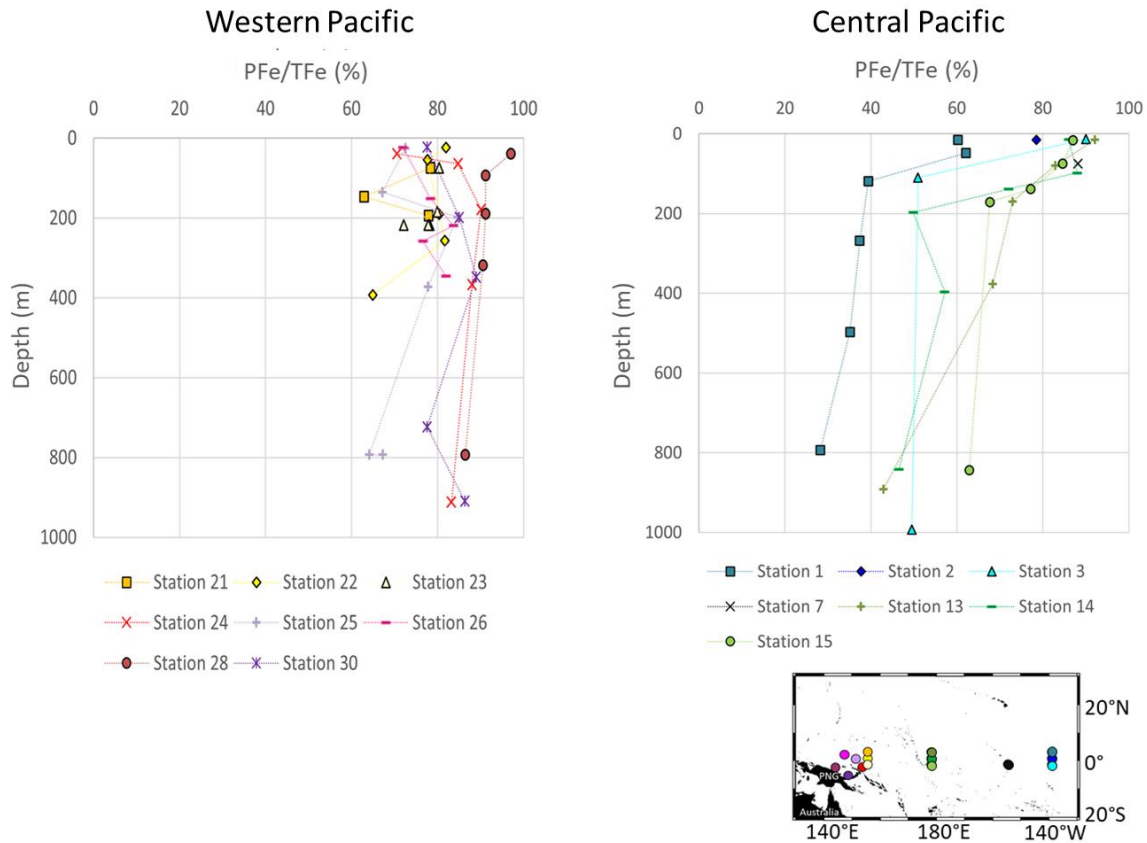
16.0

Average value

11.4 ± 6.6 (2SD)

874

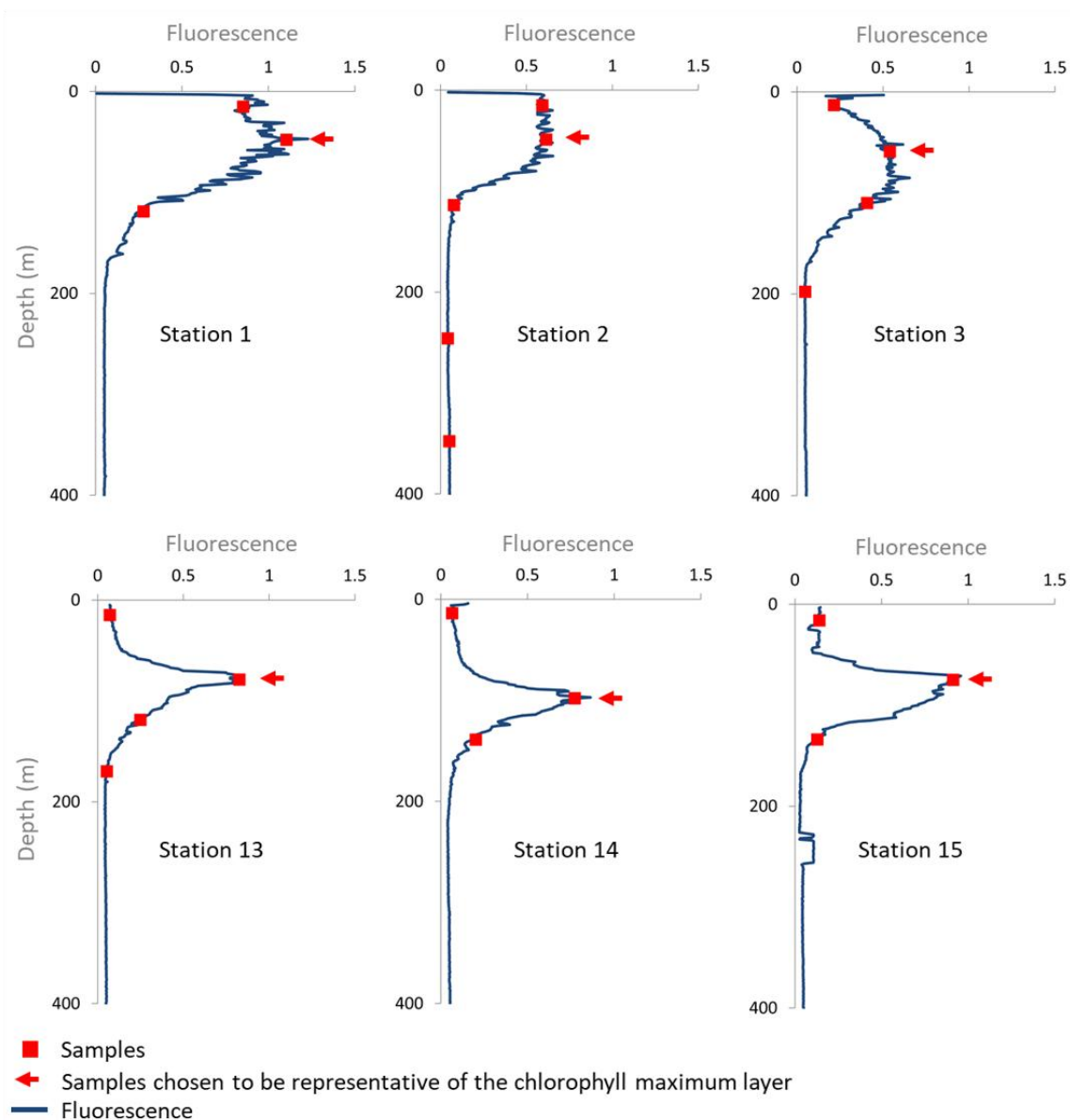
875 **Figure A1.** Fraction of particulate Fe (PFe) relative to total Fe (TFe) (% $\text{mol}\cdot\text{mol}^{-1}$) in the
876 western and central equatorial Pacific.



877

878

879 **Figure A2.** EUCFe cruise fluorescence profiles and sampling depth. Note that the fluorescence
880 profiles were measured in the closest (in time) Niskin rosette cast at the same station. Samples
881 chosen as representative of the chlorophyll maximum are shown by the (\leftarrow) symbol.



882

883 **Table A3.** Concentrations of particulate Fe and Al, dissolved Fe isotopic composition,
 884 estimated fractions of particulate phytoplanktonic and lithogenic Fe, isotopic composition of
 885 phytoplanktonic particulate Fe and the isotopic fractionation during biological uptake ($\Delta^{56}\text{Fe}_{\text{Phyto} - \text{DFe}}$)
 886 in the chlorophyll maximum layer. Uncertainties are reported as 95% confidence
 887 levels. Relative uncertainties for Fe and Al concentrations are 4.3 % (95% confidence level).

Station	Depth (m)	$\text{PFe}_{\text{total}}$ (nmol.kg^{-1})	$\delta^{56}\text{DFe}$ (‰)	PAI (nmol.kg^{-1})	$\text{PFe}_{\text{lithogenic}}$ (% mol.mol^{-1})	$\text{PFe}_{\text{phyto}}$ (% mol.mol^{-1})	$\delta^{56}\text{PFe}_{\text{phyto}}$ (‰)	$\Delta^{56}\text{Fe}_{\text{Phyto} - \text{DFe}}$ (‰)
Station 1	48	0.43	$+0.32 \pm 0.07$	0.53	61.7	38.3	$+0.54 \pm 0.19$	$+0.22 \pm 0.21$
Station 2	49	—	$+0.14 \pm 0.09$	6.65	—	—	—	—
Station 3	59	—	$+0.31 \pm 0.07$	0.67	—	—	—	—
Station 7	75	0.55	—	0.53	49.0	51.0	$+0.36 \pm 0.14$	—
Station 13	79	0.49	$+0.35 \pm 0.07$	0.15	15.2	84.8	$+0.30 \pm 0.12$	-0.05 ± 0.14
Station 14	98	0.43	$+0.58 \pm 0.07$	0.39	45.2	54.8	$+0.73 \pm 0.17$	$+0.15 \pm 0.19$
Station 15	75	0.27	—	0.22	40.4	59.6	$+0.46 \pm 0.12$	—

888

889 **DATA AVAILABILITY**

890 All the data used in this article are reported in Table 2. Fe concentration and isotope data
891 are available in the SEANOE data repository (<https://doi.org/10.17882/107774>, Lacan et al.,
892 2025) and [are](#) included in the GEOTRACES Data Product.

893

894 **AUTHORS CONTRIBUTIONS**

895 J.W.M. was the principal investigator of the EUCFe cruise. F.L. conceived the iron
896 isotope work. M.L., C.P. and FL analyzed the samples. C.C., F.L. and M.L. wrote the article.
897 All co-authors reviewed the manuscript.

898

899 **COMPETING INTERESTS**

900 The authors declare that they have no conflict of interest.

901

902 **ACKNOWLEDGES**

903 Amandine Radic is very much thanked for having carried out a part of the isotope work.
904 Jérôme Chmeleff, Frédéric Candaudap, and Aurélie Marquet are thanked for their support with
905 the ICP-MS at the *Observatoire Midi-Pyrénées*. Oguz Yigiterhan and Joseph Resing for their
906 help around the Goflo bottles. The captain and the crew of the R/V *Kilo Moana* and especially
907 the marine technicians Gabe Foreman, and Daniel Fitzgerald are acknowledged. Jay Cullen
908 from University of Victoria is thanked for lending the trace-metal rosette. This study was
909 funded by French and USA public funds. The CNRS (French National Center for Scientific
910 Research) and the University of Toulouse (France) are thanked. The EUCFe expedition on the
911 R/V *Kilo Moana* was supported by NSF OCE 0425721 (USA, James W. Murray). The Fe
912 isotope project was funded by CNRS-INSU ISOFERIX project (France, François Lacan). [Tim](#)
913 [Conway](#) and [Matthias Sieber](#) are acknowledged for their contributions to the GP15 and GP19
914 cruise data, and [Derek Vance](#) for his contributions to the GP19 cruise data; all were made
915 available through the GEOTRACES Intermediate Data Product. The three anonymous
916 reviewers are thanked for their comments, which allowed significantly improving the
917 manuscript.

918

919 **FINANCIAL SUPPORT**

920 This study was funded by French and USA public funds. The CNRS (French National
921 Center for Scientific Research) and the University of Toulouse (France) are thanked. The
922 EUCFe expedition on the R/V *Kilo Moana* was supported by NSF OCE 0425721 (USA). The
923 Fe isotope project was funded par CNRS-INSU ISOFERIX project.

924

925

926 **REFERENCES**

927 Abadie, C., Lacan, F., Radic, A., Pradoux, C., and Poitrasson, F.: Iron isotopes reveal distinct
928 dissolved iron sources and pathways in the intermediate versus deep Southern Ocean, *P Natl A*
929 *Sci USA*, 114, 858–863, <https://doi.org/10.1073/pnas.1603107114>, 2017.

- 930 Auzende, J.-M., Ishibashi, J.-I., Beaudoin, Y., Charlou, J.-L., Delteil, J., Donval, J.-P., Fouquet,
931 Y., Ildefonse, B., Kimura, H., Nishio, Y., Radford-Knoery, J., and Ruðllan, E.: Extensive
932 magmatic and hydrothermal activity documented in Manus Basin, *Eos, Transactions American*
933 *Geophysical Union*, 81, 449–453, <https://doi.org/10.1029/00EO00331>, 2000.
- 934 Bacon, M. P. and Anderson, R. F.: Distribution of thorium isotopes between dissolved and
935 particulate forms in the deep sea, *J Geophys Res-Oceans*, 87, 2045–2056,
936 <https://doi.org/10.1029/JC087iC03p02045>, 1982.
- 937 [Baldacchino, G.: Islands, archipelagos and water: Insights from New Guinea, *MGRSD*, 29, 5–](#)
938 [10, <https://doi.org/10.2478/mgrsd-2023-0050>, 2024.](https://doi.org/10.2478/mgrsd-2023-0050)
- 939 Bennett, S. A., Rouxel, O., Schmidt, K., Garbe-Schönberg, D., Statham, P. J., and German, C.
940 R.: Iron isotope fractionation in a buoyant hydrothermal plume, 5°S Mid-Atlantic Ridge,
941 *Geochim Cosmochim Acta*, 73, 5619–5634, <https://doi.org/10.1016/j.gca.2009.06.027>, 2009.
- 942 Bergquist, B. A. and Boyle, E. A.: Iron isotopes in the Amazon River system: Weathering and
943 transport signatures, *Earth Planet Sc Lett*, 248, 54–68,
944 <https://doi.org/10.1016/j.epsl.2006.05.004>, 2006.
- 945 Bingham, F. M. and Lukas, R.: The distribution of intermediate water in the western equatorial
946 Pacific during January–February 1986, *Deep-Sea Res Pt I*, 42, 1545–1573,
947 [https://doi.org/10.1016/0967-0637\(95\)00064-D](https://doi.org/10.1016/0967-0637(95)00064-D), 1995.
- 948 [Bonnet, S., Biegala, I. C., Dutrieux, P., Slemmons, L. O., and Capone, D. G.: Nitrogen fixation](#)
949 [in the western equatorial Pacific: Rates, diazotrophic cyanobacterial size class distribution, and](#)
950 [biogeochemical significance, *Global Biogeochemical Cycles*, 23,](#)
951 <https://doi.org/10.1029/2008GB003439>, 2009.
- 952 Bostock, H. C., Opdyke, B. N., and Williams, M. J. M.: Characterising the intermediate depth
953 waters of the Pacific Ocean using $\delta^{13}\text{C}$ and other geochemical tracers, *Deep-Sea Res Pt I*, 57,
954 847–859, <https://doi.org/10.1016/j.dsr.2010.04.005>, 2010.
- 955 Boyle, E. A., John, S., Abouchami, W., Adkins, J. F., Echegoyen-Sanz, Y., Ellwood, M., Flegal,
956 A. R., Fornace, K., Gallon, C., Galer, S., Gault-Ringold, M., Lacan, F., Radic, A., Rehkamper,
957 M., Rouxel, O., Sohrin, Y., Stirling, C., Thompson, C., Vance, D., Xue, Z., and Zhao, Y.:
958 GEOTRACES IC1 (BATS) contamination-prone trace element isotopes Cd, Fe, Pb, Zn, Cu,
959 and Mo intercalibration, *Limno Oceanogr-Meth*, 10, 653–665,
960 <https://doi.org/10.4319/lom.2012.10.653>, 2012.
- 961 Butt, J. and Lindstrom, E.: Currents off the east coast of New Ireland, Papua New Guinea, and
962 their relevance to regional undercurrents in the western equatorial Pacific Ocean, *J Geophys*
963 *Res-Oceans*, 99, 12503–12514, <https://doi.org/10.1029/94JC00399>, 1994.
- 964 Camin, C., Lacan, F., Pradoux, C., Labatut, M., Johansen, A., and Murray, J. W.: Iron isotopes
965 suggest significant aerosol dissolution over the Pacific Ocean, *Atmos Chem Phys*, 25, 8213–
966 8228, <https://doi.org/10.5194/acp-25-8213-2025>, 2025.
- 967 Cardinal, D., Dehairs, F., Cattaldo, T., and André, L.: Geochemistry of suspended particles in
968 the Subantarctic and Polar Frontal zones south of Australia: Constraints on export and advection
969 processes, *J Geophys Res-Oceans*, 106, 31637–31656, <https://doi.org/10.1029/2000JC000251>,
970 2001.
- 971 Ccanccapa-Cartagena, A., Chavez-Gonzales, F. D., Paredes, B., Vera, C., Gutierrez, G.,
972 Valencia, R., Lucia Paz Alcázar, A., Zyaykina, N. N., Filley, T. R., and Jafvert, C. T.: Seasonal
973 differences in trace metal concentrations in the major rivers of the hyper-arid southwestern

- 974 Andes basins of Peru, *J Environ Manage*, 344, 118493,
975 <https://doi.org/10.1016/j.jenvman.2023.118493>, 2023.
- 976 Chavez, F. P., Buck, K. R., and Barber, R. T.: Phytoplankton taxa in relation to primary
977 production in the equatorial Pacific, *Deep Sea Research Part A. Oceanographic Research*
978 *Papers*, 37, 1733–1752, [https://doi.org/10.1016/0198-0149\(90\)90074-6](https://doi.org/10.1016/0198-0149(90)90074-6), 1990.
- 979 Chisholm, S. W. and Morel, F. M. M.: What controls phytoplankton production in nutrient-rich
980 areas of the open sea?, in: *Limnology and Oceanography*, American Society of Limnology and
981 *Oceanography Symposium*, San-Marcos, California, U1507–U1511, 1991.
- 982 Coale, K. H., Fitzwater, S. E., Gordon, R. M., Johnson, K. S., and Barber, R. T.: Control of
983 community growth and export production by upwelled iron in the equatorial Pacific Ocean,
984 *Nature*, 379, 621–624, <https://doi.org/10.1038/379621a0>, 1996.
- 985 Cohen, N. R., Noble, A. E., Moran, D. M., McIlvin, M. R., Goepfert, T. J., Hawco, N. J.,
986 German, C. R., Horner, T. J., Lamborg, C. H., McCrow, J. P., Allen, A. E., and Saito, M. A.:
987 Hydrothermal trace metal release and microbial metabolism in the northeastern Lau Basin of
988 the South Pacific Ocean, *Biogeosciences*, 18, 5397–5422, [https://doi.org/10.5194/bg-18-5397-](https://doi.org/10.5194/bg-18-5397-2021)
989 2021, 2021.
- 990 Conway, T. M. and John, S. G.: Quantification of dissolved iron sources to the North Atlantic
991 Ocean, *Nature*, 511, 212–215, <https://doi.org/10.1038/nature13482>, 2014.
- 992 Conway, T. M., John, S. G., and Lacan, F.: Intercomparison of dissolved iron isotope profiles
993 from reoccupation of three GEOTRACES stations in the Atlantic Ocean, *Mar Chem*, 183, 50–
994 61, <https://doi.org/10.1016/j.marchem.2016.04.007>, 2016.
- 995 Cravatte, S., Kestenare, E., Marin, F., Dutrieux, P., and Firing, E.: Subthermocline and
996 Intermediate Zonal Currents in the Tropical Pacific Ocean: Paths and Vertical Structure, *J Phys*
997 *Oceanogr*, 47, 2305–2324, <https://doi.org/10.1175/JPO-D-17-0043.1>, 2017.
- 998 Criss, R. E.: *Principles of Stable Isotope Distribution*, Oxford University Press, Oxford, New
999 York, 264 pp., ISBN 978-0-19-756119-5, 1999.
- 1000 Dammshäuser, A.: Distribution and behavior of the lithogenic tracers aluminium and titanium
1001 in the upper water column of the Atlantic Ocean, Faculty of Mathematics and Natural Sciences
1002 Christian-Albrechts-Universität zu Kiel, [https://nbn-resolving.org/urn:nbn:de:gbv:8-diss-](https://nbn-resolving.org/urn:nbn:de:gbv:8-diss-81211)
1003 81211 (last access:16 November 2024), 2012.
- 1004 Delcroix, T., Eldin, G., Radenac, M.-H., Toole, J., and Firing, E.: Variation of the western
1005 equatorial Pacific Ocean, 1986–1988, *Journal of Geophysical Research: Oceans*, 97, 5423–
1006 5445, <https://doi.org/10.1029/92JC00127>, 1992.
- 1007 Ellwood, M. J., Hutchins, D. A., Lohan, M. C., Milne, A., Nasemann, P., Nodder, S. D., Sander,
1008 S. G., Strzepek, R., Wilhelm, S. W., and Boyd, P. W.: Iron stable isotopes track pelagic iron
1009 cycling during a subtropical phytoplankton bloom, *P Natl Acad Sci USA*, 112, E15–E20,
1010 <https://doi.org/10.1073/pnas.1421576112>, 2015.
- 1011 Ellwood, M. J., Strzepek, R. F., Strutton, P. G., Trull, T. W., Fourquez, M., and Boyd, P. W.:
1012 Distinct iron cycling in a Southern Ocean eddy, *Nat Commun*, 11, 825,
1013 <https://doi.org/10.1038/s41467-020-14464-0>, 2020.
- 1014 Emery, W. J. and Meincke, J.: Global water masses : summary and review, *Oceanol Acta*, 9,
1015 383–391, ISSN 0399-1784, 1986.

- 1016 Fantle, M. S. and DePaolo, D. J.: Iron isotopic fractionation during continental weathering,
1017 *Earth Planet Sc Lett*, 228, 547–562, <https://doi.org/10.1016/j.epsl.2004.10.013>, 2004.
- 1018 Fiedler, P. C. and Talley, L. D.: Hydrography of the eastern tropical Pacific: A review, *Prog*
1019 *Oceanogr*, 69, 143–180, <https://doi.org/10.1016/j.pocean.2006.03.008>, 2006.
- 1020 Fine, R. A., Lukas, R., Bingham, F. M., Warner, M. J., and Gammon, R. H.: The western
1021 equatorial Pacific: A water mass crossroads, *Journal of Geophysical Research: Oceans*, 99,
1022 25063–25080, <https://doi.org/10.1029/94JC02277>, 1994.
- 1023 Fitzsimmons, J. N., John, S. G., Marsay, C. M., Hoffman, C. L., Nicholas, S. L., Toner, B. M.,
1024 German, C. R., and Sherrell, R. M.: Iron persistence in a distal hydrothermal plume supported
1025 by dissolved–particulate exchange, *Nature Geosci*, 10, 195–201,
1026 <https://doi.org/10.1038/ngeo2900>, 2017.
- 1027 Flament, P., Mattielli, N., Aimoz, L., Choël, M., Deboudt, K., Jong, J. de, Rimetz-Planchon, J.,
1028 and Weis, D.: Iron isotopic fractionation in industrial emissions and urban aerosols,
1029 *Chemosphere*, 73, 1793–1798, <https://doi.org/10.1016/j.chemosphere.2008.08.042>, 2008.
- 1030 Frank, M., Eisenhauer, A., Bonn, W. J., Walter, P., Grobe, H., Kubik, P. W., Dittrich-Hannen,
1031 B., and Mangini, A.: Sediment redistribution versus paleoproductivity change: Weddell Sea
1032 margin sediment stratigraphy and biogenic particle flux of the last 250,000 years deduced from
1033 ²³⁰Thex, ¹⁰Be and biogenic barium profiles, *Earth Planet Sc Lett*, 136, 559–573,
1034 [https://doi.org/10.1016/0012-821X\(95\)00161-5](https://doi.org/10.1016/0012-821X(95)00161-5), 1995.
- 1035 [GEOTRACES Intermediate Data Product Group: The GEOTRACES Intermediate Data](https://doi.org/10.5285/42c92148-8d03-8be6-e063-7086abc09f0c)
1036 [Product 2025 \(IDP2025\)](https://doi.org/10.5285/42c92148-8d03-8be6-e063-7086abc09f0c), [https://doi:10.5285/42c92148-8d03-8be6-e063-7086abc09f0c](https://doi.org/10.5285/42c92148-8d03-8be6-e063-7086abc09f0c), [data
1037 [set\], 2025.](https://doi.org/10.5285/42c92148-8d03-8be6-e063-7086abc09f0c)
- 1038 Germineaud, C., Ganachaud, A., Sprintall, J., Cravatte, S., Eldin, G., Albery, M. S., and Privat,
1039 E.: Pathways and Water Mass Properties of the Thermocline and Intermediate Waters in the
1040 Solomon Sea, *J Phys Oceanogr*, 46, 3031–3049, <https://doi.org/10.1175/JPO-D-16-0107.1>,
1041 2016.
- 1042 Gordon, R. M., Coale, K. H., and Johnson, K. S.: Iron distributions in the equatorial Pacific:
1043 Implications for new production, *Limnol Oceanogr*, 42, 419–431,
1044 <https://doi.org/10.4319/lo.1997.42.3.0419>, 1997.
- 1045 Grenier, M.: Le rôle du pacifique tropical sud-ouest dans la fertilisation du pacifique équatorial :
1046 couplage dynamique et multi-traceur, *These de doctorat, Toulouse 3*, 205 pp.,
1047 <https://theses.hal.science/tel-00876092> (last access: 4 April 2024), 2012.
- 1048 Grenier, M., Cravatte, S., Blanke, B., Menkes, C., Koch-Larrouy, A., Durand, F., Melet, A.,
1049 and Jeandel, C.: From the western boundary currents to the Pacific Equatorial Undercurrent:
1050 Modeled pathways and water mass evolutions, *Journal of Geophysical Research: Oceans*, 116,
1051 <https://doi.org/10.1029/2011JC007477>, 2011.
- 1052 Grenier, M., Jeandel, C., Lacan, F., Vance, D., Venchiarutti, C., Cros, A., and Cravatte, S.:
1053 From the subtropics to the central equatorial Pacific Ocean: Neodymium isotopic composition
1054 and rare earth element concentration variations, *J Geophys Res-Oceans*, 118, 592–618,
1055 <https://doi.org/10.1029/2012JC008239>, 2013.
- 1056 Hayes, J.: *An Introduction to Isotopic Calculations*, Woods Hole Oceanographic Institution,
1057 <https://doi.org/10.1575/1912/27058>, 2004.

- 1058 He, Y., Kadko, D. C., Stephens, M. P., Sheridan, M. T., Buck, C. S., Marsay, C. M., Landing,
1059 W. M., Zheng, M., and Liu, P.: Constraining aerosol deposition over the global ocean, *Nat.*
1060 *Geosci.*, 18, 966–974, <https://doi.org/10.1038/s41561-025-01785-2>, 2025.
- 1061 Homoky, W. B., Severmann, S., Mills, R. A., Statham, P. J., and Fones, G. R.: Pore-fluid Fe
1062 isotopes reflect the extent of benthic Fe redox recycling: Evidence from continental shelf and
1063 deep-sea sediments, *Geology*, 37, 751–754, <https://doi.org/10.1130/G25731A.1>, 2009.
- 1064 Homoky, W. B., Conway, T. M., John, S. G., König, D., Deng, F., Tagliabue, A., and Mills, R.
1065 A.: Iron colloids dominate sedimentary supply to the ocean interior, *P Natl Acad Sci USA*, 118,
1066 e2016078118, <https://doi.org/10.1073/pnas.2016078118>, 2021.
- 1067 Ingri, J., Malinovsky, D., Rodushkin, I., Baxter, D. C., Widerlund, A., Andersson, P.,
1068 Gustafsson, Ö., Forsling, W., and Öhlander, B.: Iron isotope fractionation in river colloidal
1069 matter, *Earth Planet Sc Lett*, 245, 792–798, <https://doi.org/10.1016/j.epsl.2006.03.031>, 2006.
- 1070 John, S. G., Boyle, E. A., Cunningham, B. R., Fu, F.-X., Greene, S., Hodierne, C., Hutchins, D.
1071 A., Kavner, A., King, A. L., Rosenberg, A. D., Saito, M. A., and Wasson, A.: Kinetic Isotope
1072 Effects During Reduction of Fe(III) to Fe(II): Large Normal and Inverse Isotope Effects for
1073 Abiotic Reduction and Smaller Fractionations by Phytoplankton in Culture, *Geochemistry,*
1074 *Geophysics, Geosystems*, 25, e2023GC010952, <https://doi.org/10.1029/2023GC010952>, 2024.
- 1075 John, S. G., Mendez, J., Moffett, J., and Adkins, J.: The flux of iron and iron isotopes from San
1076 Pedro Basin sediments, *Geochim Cosmochim Ac*, 93, 14–29,
1077 <https://doi.org/10.1016/j.gca.2012.06.003>, 2012.
- 1078 John, S. G., Helgoe, J., Townsend, E., Weber, T., DeVries, T., Tagliabue, A., Moore, K., Lam,
1079 P., Marsay, C. M., and Till, C.: Biogeochemical cycling of Fe and Fe stable isotopes in the
1080 Eastern Tropical South Pacific, *Mar Chem*, 201, 66–76,
1081 <https://doi.org/10.1016/j.marchem.2017.06.003>, 2018.
- 1082 Johnson, G. C., Sloyan, B. M., Kessler, W. S., and McTaggart, K. E.: Direct measurements of
1083 upper ocean currents and water properties across the tropical Pacific during the 1990s, *Progress*
1084 *in Oceanography*, 52, 31–61, [https://doi.org/10.1016/S0079-6611\(02\)00021-6](https://doi.org/10.1016/S0079-6611(02)00021-6), 2002.
- 1085 Johnson, Z., Shyam, R., Ritchie, A., Mioni, C., Lance, V., Murray, J., and Zinser, E.: The effect
1086 of iron- and light-limitation on phytoplankton communities of deep chlorophyll maxima of the
1087 western Pacific Ocean, *Journal of Marine Research*, 68, 2010.
- 1088 Kadko, D., Landing, W. M., and Buck, C. S.: Quantifying Atmospheric Trace Element
1089 Deposition Over the Ocean on a Global Scale With Satellite Rainfall Products, *Geophysical*
1090 *Research Letters*, 47, e2019GL086357, <https://doi.org/10.1029/2019GL086357>, 2020.
- 1091 Kashino, Y., Aoyama, M., Kawano, T., Hendiarti, N., Syaefudin, Anantasena, Y., Muneyama,
1092 K., and Watanabe, H.: The water masses between Mindanao and New Guinea, *Journal of*
1093 *Geophysical Research: Oceans*, 101, 12391–12400, <https://doi.org/10.1029/95JC03797>, 1996.
- 1094 Kashino, Y., Ueki, I., Kuroda, Y., and Purwandani, A.: Ocean variability North of New Guinea
1095 derived from TRITON buoy data, *J Oceanogr*, 63, 545–559, [https://doi.org/10.1007/s10872-](https://doi.org/10.1007/s10872-007-0049-y)
1096 [007-0049-y](https://doi.org/10.1007/s10872-007-0049-y), 2007.
- 1097 Kaupp, L. J., Measures, C. I., Selph, K. E., and Mackenzie, F. T.: The distribution of dissolved
1098 Fe and Al in the upper waters of the Eastern Equatorial Pacific, *Deep-Sea Res Pt II*, 58, 296–
1099 310, <https://doi.org/10.1016/j.dsr2.2010.08.009>, 2011.

- 1100 Kineke, G. C., Woolfe, K. J., Kuehl, S. A., Milliman, J. D., Dellapenna, T. M., and Purdon, R.
1101 G.: Sediment export from the Sepik River, Papua New Guinea: evidence for a divergent
1102 sediment plume, *Cont Shelf Res*, 20, 2239–2266, [https://doi.org/10.1016/S0278-](https://doi.org/10.1016/S0278-4343(00)00069-8)
1103 4343(00)00069-8, 2000.
- 1104 Klar, J. K., Schlosser, C., Milton, J. A., Woodward, E. M. S., Lacan, F., Parkinson, I. J.,
1105 Achterberg, E. P., and James, R. H.: Sources of dissolved iron to oxygen minimum zone waters
1106 on the Senegalese continental margin in the tropical North Atlantic Ocean: Insights from iron
1107 isotopes, *Geochim Cosmochim Acta*, 236, 60–78, <https://doi.org/10.1016/j.gca.2018.02.031>,
1108 2018.
- 1109 Kuehl, S. A., Brunskill, G. J., Burns, K., Fugate, D., Kniskern, T., and Meneghini, L.: Nature
1110 of sediment dispersal off the Sepik River, Papua New Guinea: preliminary sediment budget and
1111 implications for margin processes, *Cont Shelf Res*, 24, 2417–2429,
1112 <https://doi.org/10.1016/j.csr.2004.07.016>, 2004.
- 1113 Kurisu, M., Sakata, K., Miyamoto, C., Takaku, Y., Iizuka, T., and Takahashi, Y.: Variation of
1114 Iron Isotope Ratios in Anthropogenic Materials Emitted through Combustion Processes, *Chem*
1115 *Lett*, 45, 970–972, <https://doi.org/10.1246/cl.160451>, 2016.
- 1116 Labatut, M., Lacan, F., Pradoux, C., Chmeleff, J., Radic, A., Murray, J. W., Poitrasson, F.,
1117 Johansen, A. M., and Thil, F.: Iron sources and dissolved-particulate interactions in the seawater
1118 of the Western Equatorial Pacific, iron isotope perspectives, *Global Biogeochem Cy*, 28, 1044–
1119 1065, <https://doi.org/10.1002/2014GB004928>, 2014.
- 1120 Lacan, F. and Jeandel, C.: Tracing Papua New Guinea imprint on the central Equatorial Pacific
1121 Ocean using neodymium isotopic compositions and Rare Earth Element patterns, *Earth Planet*
1122 *Sc Lett*, 186, 497–512, [https://doi.org/10.1016/S0012-821X\(01\)00263-1](https://doi.org/10.1016/S0012-821X(01)00263-1), 2001.
- 1123 [Lacan, F. and Jeandel, C.: Neodymium isotopes as a new tool for quantifying exchange fluxes](#)
1124 [at the continent–ocean interface, *Earth and Planetary Science Letters*, 232, 245–257,](#)
1125 <https://doi.org/10.1016/j.epsl.2005.01.004>, 2005.
- 1126 Lacan, F., Radic, A., Jeandel, C., Poitrasson, F., Sarthou, G., Pradoux, C., and Freydier, R.:
1127 Measurement of the isotopic composition of dissolved iron in the open ocean, *Geophys Res*
1128 *Lett*, 35, L24610, <https://doi.org/10.1029/2008GL035841>, 2008.
- 1129 Lacan, F., Radic, A., Labatut, M., Jeandel, C., Poitrasson, F., Sarthou, G., Pradoux, C.,
1130 Chmeleff, J., and Freydier, R.: High-Precision Determination of the Isotopic Composition of
1131 Dissolved Iron in Iron Depleted Seawater by Double Spike Multicollector-ICPMS, *Anal Chem*,
1132 82, 7103–7111, <https://doi.org/10.1021/ac1002504>, 2010.
- 1133 Lacan, F., Artigue, L., Klar, J. K., Pradoux, C., Chmeleff, J., and Freydier, R.: Interferences
1134 and Matrix Effects on Iron Isotopic Composition Measurements by ⁵⁷Fe-⁵⁸Fe Double-Spike
1135 Multi-Collector Inductively Coupled Plasma Mass Spectrometry; the Importance of Calcium
1136 and Aluminum Interferences, *Front Environ Chem*, 2,
1137 <https://doi.org/10.3389/fenvc.2021.692025>, 2021.
- 1138 Lacan, F., Pradoux, C., Dutrieux, P., Murray, J. W., Johansen, A., Radic, A., and Labatut, M.:
1139 CTD, dissolved oxygen concentrations, iron concentrations and isotopic compositions in the
1140 filtered seawater, seawater suspended particles and aerosols, during the EUCFe cruise,
1141 KM0625, in the Equatorial Pacific Ocean, SEANOE [data set],
1142 <https://doi.org/10.17882/107774>, 2025.
- 1143 [Landry, M. R., Kirshtein, J., and Constantinou, J.: Abundances and distributions of](#)
1144 [picoplankton populations in the central equatorial Pacific from 12°N to 12°S, 140°W, *Deep Sea*](#)

- 1145 Research Part II: Topical Studies in Oceanography, 43, 871–890, <https://doi.org/10.1016/0967->
1146 0645(96)00018-5, 1996.
- 1147 Lory, C., Van Wambeke, F., Fourquez, M., Barani, A., Guieu, C., Tilliette, C., Marie, D.,
1148 Nunige, S., Berman-Frank, I., and Bonnet, S.: Assessing the contribution of diazotrophs to
1149 microbial Fe uptake using a group specific approach in the Western Tropical South Pacific
1150 Ocean, *ISME Commun*, 2, 41, <https://doi.org/10.1038/s43705-022-00122-7>, 2022.
- 1151 Mackey, D. J., O’Sullivan, J. E. Os., and Watson, R. J.: Iron in the western Pacific: a riverine
1152 or hydrothermal source for iron in the Equatorial Undercurrent?, *Deep-Sea Res Pt I*, 49, 877–
1153 893, [https://doi.org/10.1016/S0967-0637\(01\)00075-9](https://doi.org/10.1016/S0967-0637(01)00075-9), 2002.
- 1154 Marchetti, A., Varela, D. E., Lance, V. P., Lance, V. P., Palmucci, M., Giordano, M., and
1155 Virginia Armbrust, E.: Iron and silicic acid effects on phytoplankton productivity, diversity,
1156 and chemical composition in the central equatorial Pacific Ocean, *Limnology and*
1157 *Oceanography*, 55, 11–29, <https://doi.org/10.4319/lo.2010.55.1.0011>, 2010.
- 1158 Marsay, C. M., Lam, P. J., Heller, M. I., Lee, J.-M., and John, S. G.: Distribution and isotopic
1159 signature of ligand-leachable particulate iron along the GEOTRACES GP16 East Pacific Zonal
1160 Transect, *Mar Chem*, 201, 198–211, <https://doi.org/10.1016/j.marchem.2017.07.003>, 2018.
- 1161 Martin, J. H.: Iron as a Limiting Factor in Oceanic Productivity, in: *Primary Productivity and*
1162 *Biogeochemical Cycles in the Sea*, edited by: Falkowski, P. G., Woodhead, A. D., and Vivirito,
1163 K., Springer, Boston, MA, 123–137, https://doi.org/10.1007/978-1-4899-0762-2_8, 1992.
- 1164 McCartney, M. S.: Subantarctic Mode Water, Woods Hole Oceanographic Institution
1165 Contribution 3773, 103–119,
1166 <https://www.whoi.edu/science/PO/people/mmccartney/pdfs/McCartney77.pdf> (last access: 15
1167 January 2025), 1977.
- 1168 McManus, J., Berelson, W. M., Hammond, D. E., and Klinkhammer, G. P.: Barium Cycling in
1169 the North Pacific: Implications for the Utility of Ba as a Paleoproductivity and Paleoalkalinity
1170 Proxy, *Paleoceanography*, 14, 53–61, <https://doi.org/10.1029/1998PA900007>, 1999.
- 1171 Milliman, J. D.: Sediment discharge to the ocean from small mountainous rivers: The New
1172 Guinea example, *Geo-Mar Lett*, 15, 127–133, <https://doi.org/10.1007/BF01204453>, 1995.
- 1173 Milliman, J. D. and Syvitski, J. P. M.: Geomorphic/Tectonic Control of Sediment Discharge to
1174 the Ocean: The Importance of Small Mountainous Rivers, *The Journal of Geology*, 100, 525–
1175 544, <https://doi.org/10.1086/629606>, 1992.
- 1176 Milliman, J. D., Farnsworth, K. L., and Albertin, C. S.: Flux and fate of fluvial sediments
1177 leaving large islands in the East Indies, *J Sea Res*, 41, 97–107, <https://doi.org/10.1016/S1385->
1178 1101(98)00040-9, 1999.
- 1179 Morel, F. M. M., Lam, P. J., and Saito, M. A.: Trace Metal Substitution in Marine
1180 Phytoplankton, *Annu Rev Earth Pl Sc*, 48, 491–517, <https://doi.org/10.1146/annurev-earth->
1181 053018-060108, 2020.
- 1182 Mulholland, D. S., Poitrasson, F., Shirokova, L. S., González, A. G., Pokrovsky, O. S.,
1183 Boaventura, G. R., and Vieira, L. C.: Iron isotope fractionation during Fe(II) and Fe(III)
1184 adsorption on cyanobacteria, *Chemical Geology*, 400, 24–33,
1185 <https://doi.org/10.1016/j.chemgeo.2015.01.017>, 2015.

- 1186 Murray, J. W., Barber, R. T., Roman, M. R., Bacon, M. P., and Feely, R. A.: Physical and
1187 Biological Controls on Carbon Cycling in the Equatorial Pacific, *Science*, 266, 58–65,
1188 <https://doi.org/10.1126/science.266.5182.58>, 1994.
- 1189 Murray, R. W., Leinen, M., and Isern, A. R.: Biogenic flux of Al to sediment in the central
1190 equatorial Pacific Ocean: Evidence for increased productivity during glacial periods,
1191 *Paleoceanography*, 8, 651–670, <https://doi.org/10.1029/93PA02195>, 1993.
- 1192 Nozaki, Y. and Alibo, D. S.: Dissolved rare earth elements in the Southern Ocean, southwest
1193 of Australia: Unique patterns compared to the South Atlantic data, *Geochem J*, 37, 47–62,
1194 <https://doi.org/10.2343/geochemj.37.47>, 2003.
- 1195 Nozaki, Y., Yang, H.-S., and Yamada, M.: Scavenging of thorium in the ocean, *J Geophys Res-*
1196 *Oceans*, 92, 772–778, <https://doi.org/10.1029/JC092iC01p00772>, 1987.
- 1197 Philander, S. G. H.: equatorial undercurrent: Measurements and theories, *Rev Geophys*, 11,
1198 513–570, <https://doi.org/10.1029/RG011i003p00513>, 1973.
- 1199 Pickard, G. L. and Emery, W. J.: *Descriptive Physical Oceanography*, Elsevier, 348 pp., ISBN
1200 978-0-7506-2759-7, 1990.
- 1201 Poitrasson, F.: On the iron isotope homogeneity level of the continental crust, *Chem Geol*, 235,
1202 195–200, <https://doi.org/10.1016/j.chemgeo.2006.06.010>, 2006.
- 1203 Pollard, R. T., Griffiths, M. J., Cunningham, S. A., Read, J. F., Pérez, F. F., and Ríos, A. F.:
1204 Vivaldi 1991 - A study of the formation, circulation and ventilation of Eastern North Atlantic
1205 Central Water, *Prog Oceanogr*, [https://doi.org/10.1016/S0079-6611\(96\)00008-0](https://doi.org/10.1016/S0079-6611(96)00008-0), 1996.
- 1206 Qu, T. and Lindstrom, E. J.: A Climatological Interpretation of the Circulation in the Western
1207 South Pacific, *J Phys Oceanogr*, 32, 2492–2508, [https://doi.org/10.1175/1520-0485\(2002\)032<2492:ACIOTC>2.0.CO;2](https://doi.org/10.1175/1520-0485(2002)032<2492:ACIOTC>2.0.CO;2), 2002.
- 1209 Qu, T. and Lindstrom, E. J.: Northward Intrusion of Antarctic Intermediate Water in the
1210 Western Pacific, *J Phys Oceanogr*, 34, 2104–2118, [https://doi.org/10.1175/1520-0485\(2004\)034<2104:NIOAIW>2.0.CO;2](https://doi.org/10.1175/1520-0485(2004)034<2104:NIOAIW>2.0.CO;2), 2004.
- 1212 Qu, T., Gao, S., Fukumori, I., Fine, R. A., and Lindstrom, E. J.: Origin and Pathway of
1213 Equatorial 13°C Water in the Pacific Identified by a Simulated Passive Tracer and Its Adjoint,
1214 *J Phys Oceanogr*, 39, 1836–1853, <https://doi.org/10.1175/2009JPO4045.1>, 2009.
- 1215 Radic, A., Lacan, F., and Murray, J. W.: Iron isotopes in the seawater of the equatorial Pacific
1216 Ocean: New constraints for the oceanic iron cycle, *Earth Planet Sc Lett*, 306, 1–10,
1217 <https://doi.org/10.1016/j.epsl.2011.03.015>, 2011.
- 1218 Renagi, O., Ridd, P., and Stieglitz, T.: Quantifying the suspended sediment discharge to the
1219 ocean from the Markham River, Papua New Guinea, *Cont Shelf Res*, 30, 1030–1041,
1220 <https://doi.org/10.1016/j.csr.2010.01.015>, 2010.
- 1221 Rodgers, K. B., Blanke, B., Madec, G., Aumont, O., Ciais, P., and Dutay, J.-C.: Extratropical
1222 sources of Equatorial Pacific upwelling in an OGCM, *Geophys Res Lett*, 30,
1223 <https://doi.org/10.1029/2002GL016003>, 2003.
- 1224 Rousseau, T. C. C., Sonke, J. E., Chmeleff, J., van Beek, P., Souhaut, M., Boaventura, G.,
1225 Seyler, P., and Jeandel, C.: Rapid neodymium release to marine waters from lithogenic
1226 sediments in the Amazon estuary, *Nat Commun*, 6, 7592, <https://doi.org/10.1038/ncomms8592>,
1227 2015.

- 1228 Rouxel, O., Shanks, W. C., Bach, W., and Edwards, K. J.: Integrated Fe- and S-isotope study
1229 of seafloor hydrothermal vents at East Pacific Rise 9–10°N, *Chemical Geology*, 252, 214–227,
1230 <https://doi.org/10.1016/j.chemgeo.2008.03.009>, 2008.
- 1231 Rudnick, R. L. and Gao, S.: 4.1 - Composition of the Continental Crust, in: *Treatise on*
1232 *Geochemistry (Second Edition)*, edited by: Holland, H. D. and Turekian, K. K., Elsevier,
1233 Oxford, 1–51, <https://doi.org/10.1016/B978-0-08-095975-7.00301-6>, 2014.
- 1234 Ryan, J. P., Ueki, I., Chao, Y., Zhang, H., Polito, P. S., and Chavez, F. P.: Western Pacific
1235 modulation of large phytoplankton blooms in the central and eastern equatorial Pacific, *Journal*
1236 *of Geophysical Research: Biogeosciences*, 111, <https://doi.org/10.1029/2005JG000084>, 2006.
- 1237 Sarthou, G., Bucciarelli, E., Quéroué, F., Lacan, F., Planquette, H., Pham, V. Q., Grand, M.,
1238 Pradoux, C., Rodier, M., Bonnet, S., Eldin, G., Cravatte, S., Jeandel, C., and Ganachaud, A.:
1239 Dissolved iron distribution and budget in the Solomon Sea, *Marine Chemistry*, 273, 104567,
1240 <https://doi.org/10.1016/j.marchem.2025.104567>, 2025.
- 1241 Severmann, S., Johnson, C. M., Beard, B. L., German, C. R., Edmonds, H. N., Chiba, H., and
1242 Green, D. R. H.: The effect of plume processes on the Fe isotope composition of hydrothermally
1243 derived Fe in the deep ocean as inferred from the Rainbow vent site, Mid-Atlantic Ridge,
1244 36°14'N, *Earth Planet Sc Lett*, 225, 63–76, <https://doi.org/10.1016/j.epsl.2004.06.001>, 2004.
- 1245 Severmann, S., Johnson, C. M., Beard, B. L., and McManus, J.: The effect of early diagenesis
1246 on the Fe isotope compositions of porewaters and authigenic minerals in continental margin
1247 sediments, *Geochim Cosmochim Acta*, 70, 2006–2022,
1248 <https://doi.org/10.1016/j.gca.2006.01.007>, 2006.
- 1249 Sharma, M., Polizzotto, M., and Anbar, A. D.: Iron isotopes in hot springs along the Juan de
1250 Fuca Ridge, *Earth Planet Sc Lett*, 194, 39–51, [https://doi.org/10.1016/S0012-821X\(01\)00538-](https://doi.org/10.1016/S0012-821X(01)00538-6)
1251 6, 2001.
- 1252 Shelley, R. U., Roca-Martí, M., Castrillejo, M., Sanial, V., Masqué, P., Landing, W. M., van
1253 Beek, P., Planquette, H., and Sarthou, G.: Quantification of trace element atmospheric
1254 deposition fluxes to the Atlantic Ocean (>40°N; GEOVIDE, GEOTRACES GA01) during
1255 spring 2014, *Deep-Sea Res Pt I*, 119, 34–49, <https://doi.org/10.1016/j.dsr.2016.11.010>, 2017.
- 1256 Sieber, M., Conway, T. M., de Souza, G. F., Hassler, C. S., Ellwood, M. J., and Vance, D.:
1257 Isotopic fingerprinting of biogeochemical processes and iron sources in the iron-limited surface
1258 Southern Ocean, *Earth Planet Sc Lett*, 567, 116967, <https://doi.org/10.1016/j.epsl.2021.116967>,
1259 2021.
- 1260 Sieber, M., Lanning, N. T., Steffen, J. M., Bian, X., Yang, S.-C., Lee, J. M., Weiss, G., Hunt,
1261 H. R., Charette, M. A., Moore, W. S., Hautala, S. L., Hatta, M., Lam, P. J., John, S. G.,
1262 Fitzsimmons, J. N., and Conway, T. M.: Long Distance Transport of Subsurface Sediment-
1263 Derived Iron From Asian to Alaskan Margins in the North Pacific Ocean, *Geophys Res Lett*,
1264 51, e2024GL110836, <https://doi.org/10.1029/2024GL110836>, 2024.
- 1265 Slemons, L., Gorgues, T., Aumont, O., Menkes, C., and Murray, J. W.: Biogeochemical impact
1266 of a model western iron source in the Pacific Equatorial Undercurrent, *Deep Sea Research Part*
1267 *I: Oceanographic Research Papers*, 56, 2115–2128, <https://doi.org/10.1016/j.dsr.2009.08.005>,
1268 2009.
- 1269 Slemons, L., Murray, J. W., Resing, J., Paul, B., and Dutrieux, P.: Western Pacific coastal
1270 sources of iron, manganese, and aluminum to the Equatorial Undercurrent, *Global Biogeochem*
1271 *Cy*, 24, <https://doi.org/10.1029/2009GB003693>, 2010.

- 1272 Slemons, L., Paul, B., Resing, J., and Murray, J. W.: Particulate iron, aluminum, and manganese
 1273 in the Pacific equatorial undercurrent and low latitude western boundary current sources, *Mar*
 1274 *Chem*, 142–144, 54–67, <https://doi.org/10.1016/j.marchem.2012.08.003>, 2012.
- 1275 Sofen, L. E., Antipova, O. A., Buck, K. N., Caprara, S., Chacho, L., Johnson, R. J., Kim, G.,
 1276 Morton, P., Ohnemus, D. C., Rauschenberg, S., Sedwick, P. N., Tagliabue, A., and Twining, B.
 1277 S.: Authigenic Iron Is a Significant Component of Oceanic Labile Particulate Iron Inventories,
 1278 *Global Biogeochemical Cycles*, 37, e2023GB007837, <https://doi.org/10.1029/2023GB007837>,
 1279 2023.
- 1280 Sokolov, S. and Rintoul, S.: Circulation and water masses of the southwest Pacific: WOCE
 1281 Section P11, Papua New Guinea to Tasmania, *J Mar Res*, 58, 2000.
- 1282 Stramma, L. and England, M. H.: On the water masses and mean circulation of the South
 1283 Atlantic Ocean, *J Geophys Res-Oceans*, 104, 20863–20883,
 1284 <https://doi.org/10.1029/1999JC900139>, 1999.
- 1285 Sutak, R., Camadro, J.-M., and Lesuisse, E.: Iron Uptake Mechanisms in Marine
 1286 Phytoplankton, *Front. Microbiol.*, 11, <https://doi.org/10.3389/fmicb.2020.566691>, 2020.
- 1287 Swanner, E. D., Bayer, T., Wu, W., Hao, L., Obst, M., Sundman, A., Byrne, J. M., Michel, F.
 1288 M., Kleinhanns, I. C., Kappler, A., and Schoenberg, R.: Iron Isotope Fractionation during Fe(II)
 1289 Oxidation Mediated by the Oxygen-Producing Marine Cyanobacterium *Synechococcus* PCC
 1290 7002, *Environ Sci Technol*, 51, 4897–4906, <https://doi.org/10.1021/acs.est.6b05833>, 2017.
- 1291 Tagliabue, A., Buck, K. N., Sofen, L. E., Twining, B. S., Aumont, O., Boyd, P. W., Caprara,
 1292 S., Homoky, W. B., Johnson, R., König, D., Ohnemus, D. C., Sohst, B., and Sedwick, P.:
 1293 Authigenic mineral phases as a driver of the upper-ocean iron cycle, *Nature*, 620, 104–109,
 1294 <https://doi.org/10.1038/s41586-023-06210-5>, 2023.
- 1295 Talley, L. D.: Some aspects of ocean heat transport by the shallow, intermediate and deep
 1296 overturning circulations, *Geoph Monog Series*, 112, 1–22,
 1297 <https://doi.org/10.1029/GM112p0001>, 1999.
- 1298 Talley, L. D.: Freshwater transport estimates and the global overturning circulation: Shallow,
 1299 deep and throughflow components, *Prog Oceanogr*, 78, 257–303,
 1300 <https://doi.org/10.1016/j.pocean.2008.05.001>, 2008.
- 1301 Talley, L. D., Pickard, G. L., Emery, W. J., and Swift, J. H.: *Descriptive Physical*
 1302 *Oceanography: An Introduction*, Academic Press, 555 pp., ISBN 978-0-7506-4552-2, 2011.
- 1303 Tian, H.-A., van Manen, M., Bunnell, Z. B., Jung, J., Lee, S. H., Kim, T.-W., Reichart, G.-J.,
 1304 Conway, T. M., and Middag, R.: Biogeochemistry of iron in coastal Antarctica: isotopic
 1305 insights for external sources and biological uptake in the Amundsen Sea polynyas, *Geochim*
 1306 *Cosmochim Acta*, 363, 51–67, <https://doi.org/10.1016/j.gca.2023.10.029>, 2023.
- 1307 Tiangang, W., Kumul, C., Yuhao, Z., Mosusu, N., Bimin, Z., Pei, N., and De Vivo, B.: National-
 1308 scale Geochemical Baseline of 69 elements in Papua New Guinea stream sediments, *J Geochem*
 1309 *Explor*, 256, 107355, <https://doi.org/10.1016/j.gexplo.2023.107355>, 2024.
- 1310 Tomczak, M. and Godfrey, J. S.: *Regional Oceanography: An Introduction*, Daya Publishing
 1311 House, 410 pp., ISBN 978-81-7035-306-5, 2003.
- 1312 Tomczak, M. and Hao, D.: Water masses in the thermocline of the coral sea, *Deep-Sea Res*, 36,
 1313 1503–1514, [https://doi.org/10.1016/0198-0149\(89\)90054-X](https://doi.org/10.1016/0198-0149(89)90054-X), 1989.

- 1314 Tsuchiya, M.: The Origin of the Pacific Equatorial 13°C Water, *J Phys Oceanogr*, 11, 794–812,
1315 [https://doi.org/10.1175/1520-0485\(1981\)011<0794:TOOTPE>2.0.CO;2](https://doi.org/10.1175/1520-0485(1981)011<0794:TOOTPE>2.0.CO;2), 1981.
- 1316 Tsuchiya, M.: Flow path of the Antarctic Intermediate Water in the western equatorial South
1317 Pacific Ocean, *Deep-Sea Res*, 38, S273–S279, [https://doi.org/10.1016/S0198-0149\(12\)80013-](https://doi.org/10.1016/S0198-0149(12)80013-6)
1318 6, 1991.
- 1319 Tsuchiya, M. and Talley, L.: Water-property distributions along an eastern Pacific
1320 hydrographic section at 135W, *J Mar Res*, 54,
1321 https://elischolar.library.yale.edu/journal_of_marine_research/2191 (last access: 4 March
1322 2024), 1996.
- 1323 Tsuchiya, M., Lukas, R., Fine, R. A., Firing, E., and Lindstrom, E.: Source waters of the Pacific
1324 Equatorial Undercurrent, *Prog Oceanogr*, 23, 101–147, [https://doi.org/10.1016/0079-](https://doi.org/10.1016/0079-6611(89)90012-8)
1325 6611(89)90012-8, 1989.
- 1326 Waeles, M., Baker, A. R., Jickells, T., and Hoogewerff, J.: Global dust teleconnections: aerosol
1327 iron solubility and stable isotope composition, *Environ Chem*, 4, 233,
1328 <https://doi.org/10.1071/EN07013>, 2007.
- 1329 Wilson, E. L., Harpp, K. S., Schwartz, D. M., and Van Kirk, R.: The Geochemical Evolution
1330 of Santa Cruz Island, Galápagos Archipelago, *Front Earth Sci*, 10,
1331 <https://doi.org/10.3389/feart.2022.845544>, 2022.
- 1332 Winckler, G., Anderson, R. F., Jaccard, S. L., and Marcantonio, F.: Ocean dynamics, not dust,
1333 have controlled equatorial Pacific productivity over the past 500,000 years, *P Natl Acad Sci*
1334 USA, 113, 6119–6124, <https://doi.org/10.1073/pnas.1600616113>, 2016.
- 1335 Wyrski, K.: The Subsurface Water Masses in the Western South Pacific Ocean, *Mar Freshwater*
1336 *Res*, 13, 18–47, <https://doi.org/10.1071/mf9620018>, 1962.
- 1337 [Xiang, Y. and Lam, P. J.: Size-Fractionated Compositions of Marine Suspended Particles in the](#)
1338 [Western Arctic Ocean: Lateral and Vertical Sources, *Journal of Geophysical Research: Oceans*,](#)
1339 [125, e2020JC016144, <https://doi.org/10.1029/2020JC016144>, 2020.](#)
- 1340 Yeghicheyan, D., Bossy, C., Bouhnik Le Coz, M., Douchet, C., Granier, G., Heimbürger, A.,
1341 Lacan, F., Lanzanova, A., Rousseau, T. C. C., Seidel, J.-L., Tharaud, M., Candaudap, F.,
1342 Chmeleff, J., Cloquet, C., Delpoux, S., Labatut, M., Losno, R., Pradoux, C., Sivry, Y., and
1343 Sonke, J. E.: A Compilation of Silicon, Rare Earth Element and Twenty-One other Trace
1344 Element Concentrations in the Natural River Water Reference Material SLRS-5 (NRC-CNRC),
1345 *Geostand Geoanal Res*, 37, 449–467, <https://doi.org/10.1111/j.1751-908X.2013.00232.x>, 2013.
- 1346 Yeghicheyan, D., Aubert, D., Bouhnik-Le Coz, M., Chmeleff, J., Delpoux, S., Djouraev, I.,
1347 Granier, G., Lacan, F., Piro, J.-L., Rousseau, T., Cloquet, C., Marquet, A., Menniti, C., Pradoux,
1348 C., Freydier, R., Vieira da Silva-Filho, E., and Suchorski, K.: A New Interlaboratory
1349 Characterisation of Silicon, Rare Earth Elements and Twenty-Two Other Trace Element
1350 Concentrations in the Natural River Water Certified Reference Material SLRS-6 (NRC-
1351 CNRC), *Geostand Geoanal Res*, 43, 475–496, <https://doi.org/10.1111/ggr.12268>, 2019.
- 1352 Yuan, X. and Talley, L. D.: Shallow Salinity Minima in the North Pacific, *J Phys Oceanogr*,
1353 22, 1302–1316, [https://doi.org/10.1175/1520-0485\(1992\)022<1302:SSMITN>2.0.CO;2](https://doi.org/10.1175/1520-0485(1992)022<1302:SSMITN>2.0.CO;2), 1992.
- 1354 Zheng, L. and Sohrin, Y.: Major lithogenic contributions to the distribution and budget of iron
1355 in the North Pacific Ocean, *Sci Rep*, 9, 11652, <https://doi.org/10.1038/s41598-019-48035-1>,
1356 2019.